

ABSTRACT

Title of Document: ENHANCEMENT OF AN INDIUM PHOSPHIDE RESONATOR SENSOR MICROSYSTEM THROUGH THE DEVELOPMENT OF AN ADAPTIVE FEEDBACK CIRCUIT AND ELECTROSPRAY DEPOSITION

Xiao Zhu Fan, Masters of Science, 2009

Directed By: Dr. Reza Ghodssi, Electrical and Computer Engineering

Cantilever resonator sensor enhancement through the development of an adaptive feedback circuit and the use of electrospray deposition is presented. The feedback system adapts to a wide range of resonators by implementing a hill climbing algorithm, locking onto the cantilever's resonance condition. Eight different cantilever-based sensors (Length=40-75 μ m), resonating at 201.0kHz to 592.1kHz, with a minimum standard deviation of 11.8Hz, corresponding to a mass resolution limit of 123fg for the device, have been dynamically detected using a single circuit. Electrospray deposition of thin-films on multiple substrate materials and released microstructures has been performed. An average deposition rate of 9.5 \pm 5nm/min was achieved with an average surface roughness of 4.5nm on a 197nm thick film. This technology will enable a post-processing method for depositing absorbing layers for sensing applications. With the development of these two technologies, the practical functionality of a chip-scale sensor microsystem will be more readily realized.

ENHANCEMENT OF AN INDIUM PHOSPHIDE RESONATOR SENSOR
MICROSYSTEM THROUGH THE DEVELOPMENT OF AN ADAPTIVE
FEEDBACK CIRCUIT AND ELECTROSPRAY DEPOSITION

By

Xiao Zhu Fan

Thesis submitted to the Faculty of the Graduate School of the
University of Maryland, College Park, in partial fulfillment
of the requirements for the degree of
Masters of Science
2009

Advisory Committee:
Professor Reza Ghodssi, Chair
Professor Thomas Murphy
Professor Pamela Abshire

© Copyright by
Xiao Zhu Fan
2009

Dedication

To mom and dad for everything.

Acknowledgements

The author would like to thank the committee members Prof. Pamela Abshire, Prof. Thomas Murphy, and especially my advisor, Prof. Reza Ghodssi, who provided his guidance and support throughout this degree process.

The author would also like to thank the members of the MEMS Sensors and Actuators Lab (MSAL) for all of their help, advice, and insightful inputs. The author would especially like to thank Mr. Nathan Siwak for his invaluable contribution to this project and his support as a mentor and friend, as well as Mr. Stephan Koev and Jonathan McGee for their useful discussions and suggestions.

Finally, the author wishes to acknowledge and thank the National Science Foundation CAREER Award program and Laboratory for Physical Sciences for funding this research.

Table of Contents

Dedication.....	ii
Acknowledgements.....	iii
Table of Contents.....	iv
List of Figures.....	vii
List of Tables.....	x
Chapter 1. Background and Motivation.....	1
1.1. Introduction.....	1
1.1.1. Overview.....	1
1.1.1. Thesis Accomplishments.....	3
1.2. MEMS.....	4
1.2.1. History.....	4
1.2.2. MEMS Fabrication.....	5
1.2.3. Optical MEMS.....	7
1.2.4. III-V Monolithic Integration.....	11
1.2.5. MEMS Resonator Sensors.....	14
1.3. Device Readout.....	17
1.3.1. Overview.....	17
1.3.2. Piezoresistive Readout.....	17
1.3.3. Piezoelectric Readout.....	18
1.3.4. Capacitive Readout.....	19
1.3.5. Optical Readout.....	19
1.3.6. Feedback Circuit.....	21
1.3.7. Integration.....	24
1.4. Thesis Organization.....	26
Chapter 2. Resonator.....	28
2.1. Introduction.....	28
2.2. Electrostatic Force.....	28
2.3. Cantilever Beam Theory.....	30

2.4.	Optical Modeling	34
2.5.	Discussion	37
Chapter 3.	Feedback Circuit Design.....	39
3.1.	Introduction.....	39
3.2.	Hill Climbing Algorithm.....	39
3.2.1.	Concept	39
3.2.2.	Applications in MEMS	41
3.3.	Circuit Implementation	41
3.3.1.	Overview.....	41
3.3.2.	Amplitude Detector.....	42
3.3.3.	Differentiator.....	43
3.3.4.	Logic Stage	44
3.3.5.	Integrator.....	45
3.3.6.	Voltage Controlled Oscillator.....	46
3.4.	PSPICE Simulation.....	47
3.5.	Discussion.....	49
Chapter 4.	Detection of Cantilever Resonant Frequency	51
4.1.	Overview.....	51
4.2.	Circuit Board Construction.....	53
4.3.	Experimental Setup.....	54
4.4.	Open Loop Circuit	55
4.5.	Closed Loop Circuit.....	56
4.6.	Discussion.....	60
Chapter 5.	Electrospray Deposition.....	63
5.1.	Introduction.....	63
5.2.	Concept	64
5.2.1.	Overview.....	64
5.2.2.	Current Generated in the Cone-Jet.....	67
5.2.3.	Predictions of Droplet Size	67
5.2.4.	Droplet Evaporation.....	68
5.2.5.	Droplet Charge.....	68

5.2.6. Droplet Location	69
5.3. Absorption Layer	70
5.4. Setup	72
5.5. Results.....	73
5.6. Discussion.....	77
Conclusion and Future Work.....	79
6.1. Summary of Results.....	79
6.1.1. Resonator Feedback Circuit.....	80
6.1.2. Electrospray Deposition.....	81
6.2. Future Work	82
Bibliography	85

List of Figures

Figure 1.1 Overview schematic of InP resonator sensors with feedback circuit integration and thin film receptor coating.....	2
Figure 1.2 Diagram and SEM of Texas Instruments DMD™ [24]	8
Figure 1.3 Picture of Lucent WaveStar lambdaRouner™ [25]	9
Figure 1.4 SEM imaging of GaAs MOEMS 1x2 switch [28]	11
Figure 1.5 SEM image of an in-plane 2x1 optical switch [29].....	11
Figure 1.6 Picture showing selective etching between InP and GaAs [37]	13
Figure 1.7 Diagram showing the relationship between material composition, lattice constant, and bandgap for some common III-V compound semiconductors [38].....	14
Figure 1.8 Schematic showing the principle of operation of a transducer [4]	15
Figure 1.9 Cantilever sensor detection of (left) single E. Coli cell (600fg) and (right) chemisorptions of thiols on gold (0.39ag) [4].....	16
Figure 1.10 Schematic of a piezoresistive readout method and an interfacing Wheatstone Bridge circuit [4].....	18
Figure 1.11 Schematic of a piezoelectric readout method and an interfacing differential amplifier circuit [58]	18
Figure 1.12 Schematic of a capacitive readout method and a possible interfacing circuit	19
Figure 1.13 Schematic of an optical readout method and an interfacing transimpedance amplifier circuit.....	20
Figure 1.14 A block diagram showing the components of a DRO feedback system [62].....	22
Figure 1.15 A block diagram showing the components of a PLO feedback system [61]	23
Figure 1.16 Schematic of a monolithically integrated system [66]	25
Figure 2.1 Diagram showing (left) beam position at no load condition and (right) beam bending in the z-direction at distributed load condition.....	30
Figure 2.2 Graph showing relationship between cantilever length and tip displacement for an applied voltage of 26V.	32
Figure 2.3 Schematic showing the optical coupling and waveguide misalignment between the cantilever waveguide and the collecting waveguide	34
Figure 2.4 Graph showing the relationship between cantilever misalignment and coupling loss (L=50um, H=1.4um, W=1.2um, and Gap=0.6um).....	37

Figure 2.5 Graph showing the relationship between applied voltage and the coupling loss across the gap due to electrostatic displacement ($L=50\mu\text{m}$, $H=1.4\mu\text{m}$, $W=1.2\mu\text{m}$, and $\text{Gap}=0.6\mu\text{m}$)	37
Figure 4.1 Diagram describing the hill climbing optimization algorithm used to locate the maximum amplitude at the resonant frequency.	40
Figure 4.2 Feedback circuit diagram showing four-stage circuit integrated with chemical resonator sensor	42
Figure 4.3. Circuit schematic of a precision full-wave rectifier built using two Op-Amps.	43
Figure 4.4. Circuit schematic of the logic stage comprising of a Schmitt Trigger, a T-FF wired from a J-K FF, and an RC integrator.	44
Figure 4.5 Circuit schematic of integrator	46
Figure 4.6. Hierarchical schematic of the open-loop circuit simulated in PSPICE where the input signal was simulated using amplitude modulated signal	47
Figure 4.7. PSPICE simulation result showing output at every stage of the feedback circuit	48
Figure 5.1 Block diagram of open-loop testing with the microresonator system.....	52
Figure 5.2 Block diagram of closed-loop testing after eliminating the function generator and connecting V_{out} to $V4$	52
Figure 5.3 Diagram of experimental setup	54
Figure 5.4. Output of individual stages of the feedback circuit while locked on to the resonant frequency. (a) Output of amplitude detector showing periodic peak amplitude, (b) differential signal of the amplitude detector, (c) Schmitt trigger output detecting the direction of the slope and (d) input of the VCO showing oscillation around a bias voltage.....	57
Figure 5.5. Showing a steady state signal around the resonant frequency (314kHz) of a $L=55\mu\text{m}$ $W=1.4\mu\text{m}$ and $T=1.8\mu\text{m}$ cantilever. The zoomed in graph shows the oscillatory signal around the resonant frequency, which could be calculated by applying a running average.....	58
Figure 5.6. Resonant frequency detection of cantilevers ranging from $L=40\mu\text{m}$ to $75\mu\text{m}$ together with their theoretical resonant frequency. Error bar for the theoretical values is based on $0.1\mu\text{m}$ fabrication tolerance.....	59
Figure 5.1 Diagram of electrospray deposition setup	65
Figure 3.2 Molecular structure of PMMA	71
Figure 3.3 Molecular structure of toluene.....	72
Figure 3.4 Diagram of the ESD setup with a shadow mask defining deposition patterns.....	73
Figure 3.5 Deposition of PMMA at an average rate of 9.5 nm/min on masked chips (a) 5 min (b) 10 min (c) 15 min	75

Figure 3.6 SEM images showing conformal coverage of microstructures	76
Figure 3.7 SEM image showing increased deposition at the edge of structures due to edge effects	76
Figure 3.8 Picture of PMMA deposition on various surface materials (Si, Au, and Si ₃ N ₄)	77

List of Tables

Table 2-1. Table of Variables I.....	29
Table 2-2 Table of Variables II.....	30
Table 5-1. List of Electrical Components Used.....	53
Table 3-1 Relavent parameters involved in the subprocesses of electrospray deposition [79]	66
Table 3-2. List of proposed polymers used as absorption layer (adapted from [81]).	70
Table 3-3 Material properties of PMMA	70
Table 3-4 Material properties of toluene	71
Table 3-5. List of proposed target analytes.....	72

Chapter 1. Background and Motivation

1.1. Introduction

1.1.1. Overview

The compatibility of size and fabrication processes between Micro Electromechanical Systems (MEMS) and microelectronic circuits has enabled the efficient system integration these technologies. While low-power MEMS components allow for simple, high function transducers with smaller footprints, circuit elements provide control and electrical readout [1]. Taking advantage of both technologies simultaneously can enable a variety of promising hybrid systems. A large portion of today's MEMS devices consist of resonators due to their wide range of applications, including oscillators [2], RF MEMS [3], and chemical and biological sensors [4]. While the field of MEMS resonators is rapidly advancing, circuit designers have been developing CMOS circuitry to complement these microresonators to ease system integration. Most often, circuits are designed to achieve an on-chip system without the reliance on external instrumentation, enabling the entire system to be miniaturized, portable, and autonomous [5]. CMOS circuits have been shown to optimize the system by increasing resonator displacement read-out resolution [6], enhancing the quality factor of resonators [7, 8], and compensating for parasitic capacitive effects [5] which may arise due to the use of discrete components.

Detecting the natural frequency of a resonator is an integral part of their operation in order to perform timing, generate oscillation, and sense analytes [9]. In addition, circuit integration more readily provides real-time output which enables the

development of feedback systems [10, 11], enhancing the functionality of the system. Feedback systems provide increased device sensitivity and Q factors [12], and autonomous resonant frequency tracking [13]. Although feedback circuits for resonators have been researched and developed since the early 90's, there is a lack of circuits specifically for MEMS devices that are adaptable and eliminate the need for each MEMS device to have its own unique control circuitry.

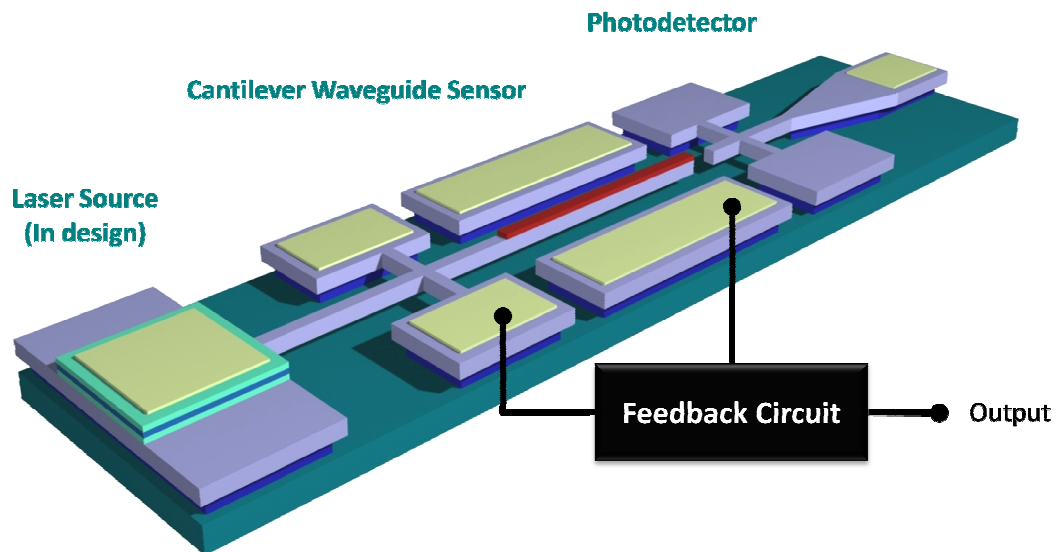


Figure 1.1 Overview schematic of InP resonator sensors with feedback circuit integration and thin film receptor coating

New fabrication technologies have also been developed in order to ensure compatibility with unconventional fabrication processes and device structures. Technologies are sometimes borrowed from other areas of research to circumvent new issues that arise with rapidly growing technology. New issues, such as device stiction and aggressive etch compatibility, need to be addressed [14]. A technology of promise and interest is that of electrospray [15], which is traditionally used for electrospray ionization [16] and colloid thrusters [17]. These technologies are used for mass spectrometry and propulsion applications, respectively. Taking advantage of

the small droplet size, electrospray deposition can be developed as a post-processing procedure for deposition of receptor layers on released microstructures to circumvent compatibility issues with other fabrication processes.

1.1.1. Thesis Accomplishments

The primary goal of this thesis was to develop of an adaptive feedback circuit that will detect the resonant frequency of resonators. The circuit design, simulation, and testing of such a system have been completed. The first implementation and utilization of the hill climbing algorithm, an optimization algorithm, for electromechanical-systems (MEMS) was also realized. These implementations have enabled a feedback system that will autonomously detect the resonant frequency of a wide range of resonators. Validation of the circuit's adaptability, by detecting a wide range of resonant frequencies of cantilever waveguides, is the first benchmark of integration with a resonator cantilever sensor system.

The secondary goal of this thesis was the development and characterization of an electrospray deposition (ESD) system used for the deposition of thin-films. An ESD setup was established, followed by characterization of the deposited film thickness, uniformity, and quality. The success of this ESD process has established a new post-fabrication process for released MEMS devices, eliminating some of the fabrication challenges when depositing an absorption layer on suspended resonator sensors.

1.2. MEMS

1.2.1. History

Microelectromechanical systems (MEMS) are traditionally defined as the technology of the integration between mechanical microdevices and electronics. These devices take advantage of batch-fabrication techniques and the economy of scale exploited by the mature integrated circuit (IC) industry. However, this field has expanded and diversified since the early 1980's, when the first microsensors were first developed, into more than just integration of mechanical microdevices and electronics, but also biological, chemical, and optical microdevices as well [1]. There are a number of forces behind the advancement of MEMS technology. One of its primary reasons is cost reduction.

Small size and batch fabrication in combination with simpler assembly allows for MEMS devices to cost orders of magnitude less than their macro counterparts. Batch fabrication allows for parallel processing, enabling high density fabrication on a single wafer using developed microfabrication processes [18].

The elimination of macro external equipment and their assembly is another reduction of cost. Traditionally, semiconductor chips can only read, process, and output electrical signals. Many functions require physical interaction, forcing electronics to be connected with bulky and expensive external transducers or actuators. While these separate systems are each proven, MEMS technology allows for their integration on the chip scale, which can provide simpler and cheaper interconnection and packaging [19].

The rapid pace of MEMS advancement is not solely driven by business. There is, in general, an advantage to size reduction as the scaling of the transduction mechanism, device design, and material properties produce favorable results. Due to the magnitude of the scaling, macroscale phenomena and intuitions may often not apply to these devices. Some potential advantages of scaling are: (1) Scaling MEMS to densities approaching the defect density of the material will increase the reliability of devices, the mechanical strength of an object is reduced only by its dimension compared to the inertial force that it can generate which is decreased by its dimension cubed. (2) Reynold's number scales with dimension causing fluid flow to become more laminar. (3) Finally, increased surface area-to-volume ratio will increase thermal transfer [1].

Finally, due their small size and low power, MEMS devices are deployable. They can be used in multi function systems such as smart dust and can be used to remotely monitor environmental conditions for military and industrial purposes. Some notable commercial successes of MEMS devices include accelerometers, gyroscopes, optical projection systems, and pressure sensors. These examples all benefit from cost and scaling advantages as described above.

1.2.2. MEMS Fabrication

One of the reasons for the rapid growth of MEMS development is due to the maturity of the IC fabrication process. Traditional MEMS devices have utilized the same materials as semiconductor computer chips not only due to compatible systems integration but also taking advantage of the research and funding that has been invested to establish the microelectronic industry. The same tools used to perform

lithography, thin-film deposition, and etching for CMOS devices are used to fabricate the mechanical elements of MEMS devices as well.

The MEMS industry has since developed some specialized fabrication processes that are tailored to MEMS devices, enabling the fabrication of 3D mechanical devices surpassing the limitations of 2D CMOS processes. These MEMS fabrication processes can be categorized into bulk micromachining and surface micromachining.

Bulk micromachining techniques refer to fabrication techniques that involve the “bulk” substrate material. Bulk micromachining can be used to form holes or trenches in the substrate. Often time, it can be used remove the substrate beneath a MEMS device, known as undercutting, in order to obtain a released free standing structure enabling physical movements. The substrate material is removed by either wet etch processes with liquid etchants or dry etch processes with vapor or plasma reactants. Specific silicon substrate removal chemistries have been developed to be compatible with CMOS processes. An example of a device fabricated using the bulk micromachining technique is the pressure sensor that utilizes a pressure sensitive membrane after the substrate beneath has been etched out.

Surface micromachining techniques refer to fabrication techniques that are done on the surface of the substrate. In order to fabricate released devices, a sacrificial layer needs to be deposited onto the substrate beneath the device and then undercut for release. In general, surface micromachining is more compatible with traditional CMOS process due to their common fabrication processes and materials

used. This method is often used for capacitive and electrostatic devices that require high resolution and control, such as the comb-drive actuator [20].

1.2.3. Optical MEMS

A subset of MEMS is optical MEMS, often known as micro-opto-electromechanical systems (MOEMS), which deals with light generation, manipulation, and detection using microstructures. As the name states, MOEMS are systems that integrate optical, electrical and mechanical functions. Optics provide great potential in the areas of data transmission, display, and sensor technologies [21].

Traditionally, the main drawback to optical communication system is the requirement for optical signal to be translated to electrical domains for switching or routing functions before they are translated back to the optical domain. These intermediate optical-electrical-optical translation stages will limit the speed of the overall system. In order to take full advantage of the speed of optical communication, optical-optical insertions are desired, eliminating any electrical conversion or processing and replaced by all-optical processing.

Most optoelectronics devices are wavelength and/or polarization dependent complicated optical-electrical processing. However, MOEMS devices offer an additional method of optical manipulation by physically altering its path. Since MOEMS device dimensions and displacement are on the same order of magnitude as the optical wavelength, they can provide great precision and accuracy. MOEMS can be divided into two main categories: free-space and guided optics.

In free-space optics, light is generally guided and steered by means of mirrors and lenses. Free-space optics is used when physical connection is impossible or

impractical, such as in the case of communication between spacecrafts or connection between very large networks. Free-space optics is required to be compatible with industry standard single mode fibers for communication applications. In order to meet standard insertion loss for telecommunication standards, free space optics components, such as microlenses, are required to prevent excessive losses from divergent propagation.

Another drawback of free space optics is the difficulty of packaging. Although free space MOEMS can increase complexity and functionality of the device, it also requires tight alignment specifications in all three dimensions. Tight specifications lead to high cost and strict fabrication tolerances [22].

An example of a free-space MOEMS is the Texas Instruments Digital Micromirror Device™ (DMD™) used in the Digital Light Processing (DLP) projection technology. The DMD chip is composed of tens of thousands of micromirrors, where each micromirror on the chip represents one display pixel. The micromirror actuator is driven between binary state, reflecting light towards and away from the pupil of the projection lens. The gray scale in between is achieved by binary pulsewidth modulation of the incident light [23].

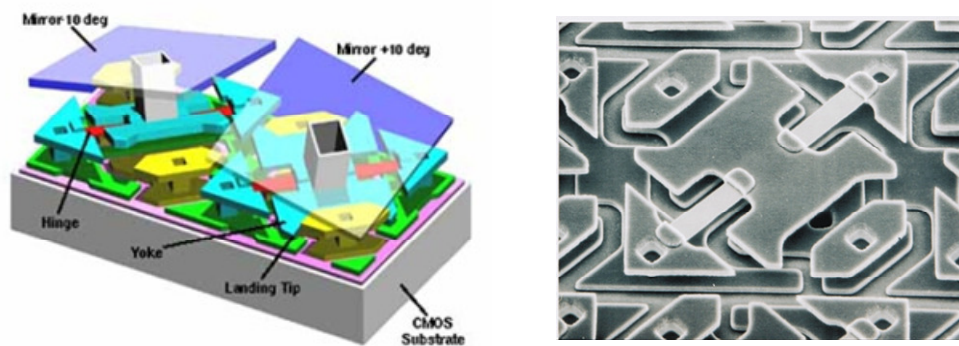


Figure 1.2 Diagram and SEM of Texas Instruments DMD™ [24]

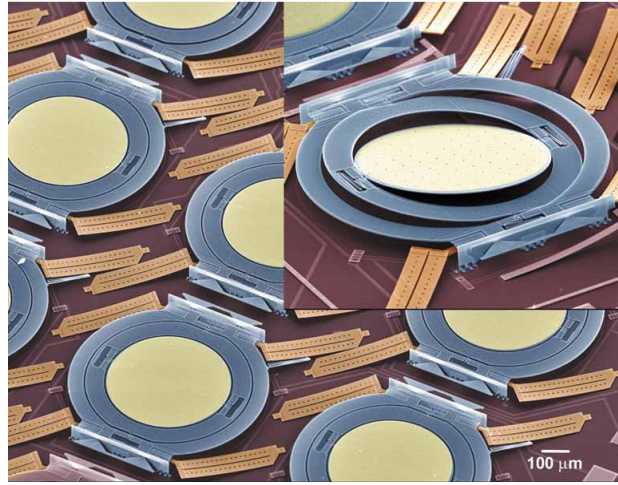


Figure 1.3 Picture of Lucent WaveStar lambdaRouter™ [25]

Lucent's WaveStar™ LambdaRouter, a 256 channel all-optical router capable of handling over 10 Tb/s of network traffic, is another MOEMS device that is based upon the principle of tilting micromirror arrays. Its analog two-axis micromirror performs non-blocking transmission through free space onto another array of positionable mirrors which then direct the beams to the output port. A Fourier lens is placed between the micromirrors to reduce the required tilt of the mirror and beam size [25].

Guided optics utilizes mechanical waveguides to determine the direction of propagation of the signal. Due to the required in-plane confinement of light, the communication channel density per chip decreases but it presents a simpler and straightforward integration and packaging scheme. Optical components can all be integrated in-plane using MEMS fabrication. An edge-emitting laser, active amplifier, mechanical switches, and a tunable filter can be monolithic integrated using MEMS technologies [26].

A drawback of guided optics is the increase in optical loss. The loss associated with guided optics is dominated by waveguide sidewall and facet roughness which causes scattering loss. In general, the loss associated with free-space mirrors is much less than the scattering loss since the surface roughness is orders of magnitude smoother than the sidewall roughness.

Popular designs of 1x2 switch are shown in Figure 1.4 and Figure 1.5, where an input waveguide is actuated to couple light into two output waveguides by aligning the output and input facets. The input waveguide is actuated electrostatically. By cascading similar 1x2 switches, Ollier *et al.* [27] have demonstrated a 1x8 optical switch with an insertion loss of 1.5 dB.

The 1x2 switches shown in Figure 1.4 and Figure 1.5 are fabricated in gallium arsenide (GaAs) and indium phosphide (InP), respectively [28, 29]. MOEMS are made of various materials depending on their application or level of integration. Materials can be wide ranged, including silicon, polymers, dielectrics, and III-V materials. There is a particular interest in III-V MOEMS because of the ability to monolithically integrate active and passive optical devices.

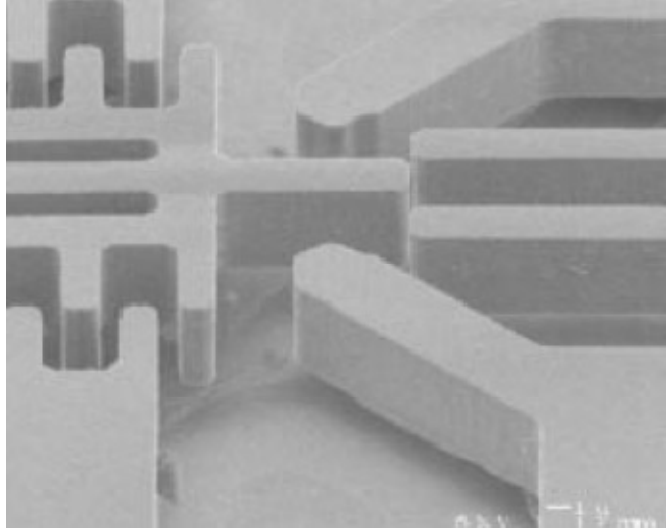


Figure 1.4 SEM imaging of GaAs MOEMS 1x2 switch [28]

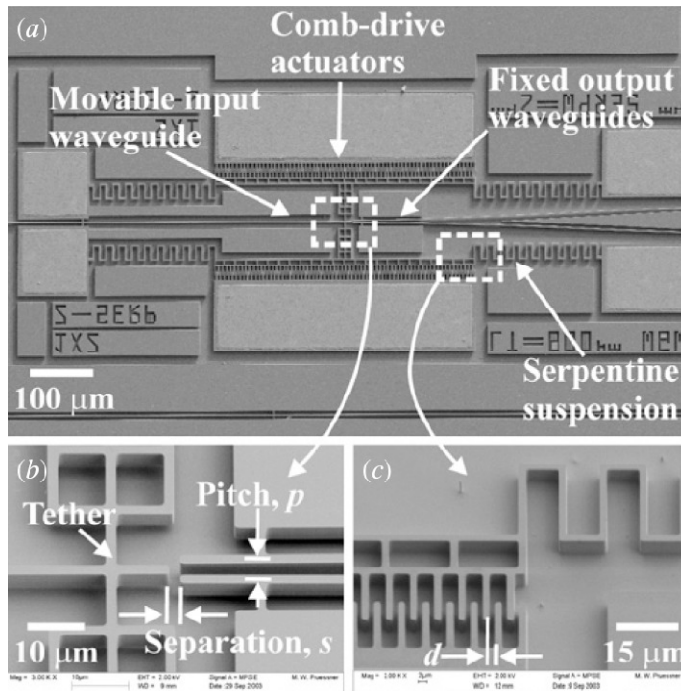


Figure 1.5 SEM image of an in-plane 2x1 optical switch [29]

1.2.4. III-V Monolithic Integration

III-V semiconductors are unconventional MEMS materials that are used because of their direct-bandgap properties [22]. Monolithic integration is a key

advantage to MEMS system integration and packaging. However, monolithic integration of active optical components is close to impossible in traditional silicon substrate due to its indirect bandgap properties. As a result, compound semiconductors from group III and group V of the periodic table, called III-V semiconductors, are used to monolithically integrate both active optical elements with passive optical elements, such as optical sources and waveguides. III-V semiconductors include InP, GaAs, InAs, InGaAsP, InSb, and GaN [30-33].

As a result the direct bandgap transition, electrons recombine with holes and efficiently emit photons, generating light. In indirect bandgap semiconductors, like silicon, direct recombination requires a change in momentum, generating phonons rather than photons [34].

In addition to having direct bandgap properties, III-V materials have positive attributes for device fabrication. The customization and the tuning ability of the material properties, such as stress, bandgap, and lattice constant, in compound semiconductors is a great advantage when using these materials. Two common growth techniques, molecular beam epitaxy (MBE) and metalorganic vapor phase epitaxy (MOVPE) [35], have been developed to control the growth and composition of these semiconductors. Below is a list of advantages due to the controlled growth and composition of III-V materials:

(i) Tuned Etch Selectivity

The composition of the grown III-V semiconductor layer can tune the etching selectivity between the layers, allowing the developments of sacrificial layers and etch stops. For example, close to 100% etch selectivity can be realized between InP

and InGaAs layers using HF:H₂O₂:H₂O (1:1:8) or H₂SO₄:H₂O₂:H₂O (1:1:20) wet etch, achieving atomic-level surface roughness and undercutting to release movable devices [36]. Taking advantage of the high selectivity, mirror like surface, and accurate thickness of epitaxial growth technique, optical filters and distributed Bragg reflectors (DBR) have been developed and demonstrated [37], see Figure 1.6.

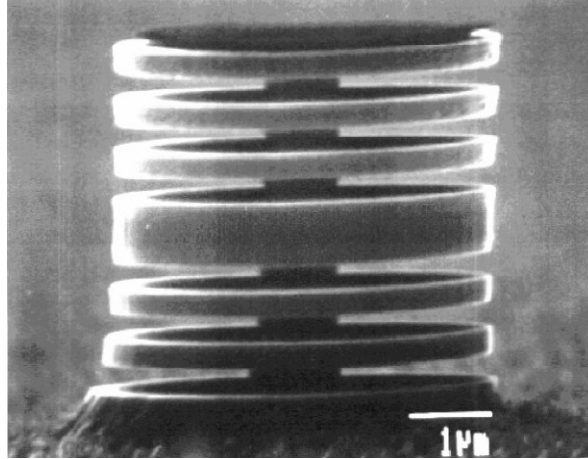


Figure 1.6 Picture showing selective etching between InP and GaAs [37]

(ii) Tuned Bandgap

MBE and MOVPE have been used to grow materials with varying bandgaps and lattice constants, as shown in Figure 1.7. Since most III-V materials are direct bandgap semiconductor compounds, they are ideal for generation, manipulation, and detection of light over a wide range of wavelength.

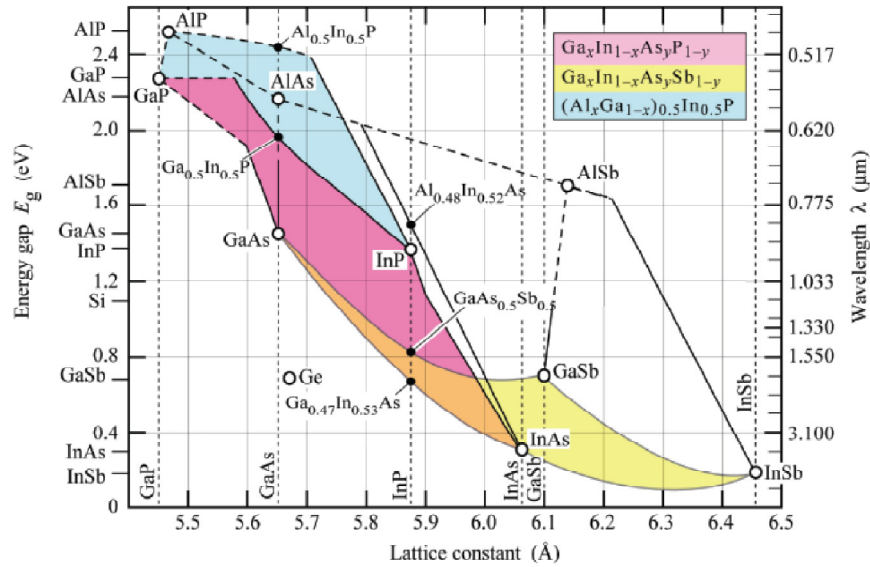


Figure 1.7 Diagram showing the relationship between material composition, lattice constant, and bandgap for some common III-V compound semiconductors [38]

(iii) Single Crystalline Growth

III-V semiconductor layers can be grown lattice matched, resulting in single-crystal device layers. The uninterrupted crystal lattice in the solid with no grain boundaries provides significant advantages on the physical and electrical properties. Increase in electron mobility, decrease in optical loss, and atomically smooth cleaved surfaces are just a few of these advantages [39]. The lattice matched growth allows multilayered lattice matched devices and lattice matched sacrificial layers, enabling single crystal released waveguides. While Bakke *et al.* [40] utilized GaAs/AlGaAs as the top waveguide layer and sacrificial layer, respectively, Pruessner *et al.* [29] and Siwak *et al.* [14] demonstrated it using InP and GaAs layers.

1.2.5. MEMS Resonator Sensors

MEMS resonator sensors are promising and developing sensor technology that combines the advantages of small size, scalability, tunability, low-powered, and

portability. The ability for the MEMS device to be mass produced and tailored to specific applications is an advantage over other sensors. Its competitors consist of using macro capacitive, resistive, bulk resonance, and optical methods to transduce the presence of the analyte into a readable signal. Some of these techniques are proven technologies that offer great sensitivity; however, they lack the ability to be easily integrated with its support equipment, limiting their use for large-scale integration and portable and deployable systems [4].

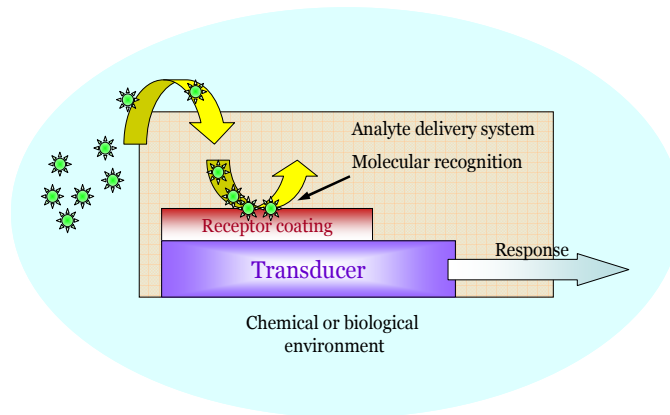


Figure 1.8 Schematic showing the principle of operation of a transducer [4]

MEMS resonator sensors were first developed in the 1960's by Nathanson [41] and Howe [42], who demonstrated vapor sensing using resonant gate transistors. The advantage of these microresonators is their ability to detect label-free analytes and be fabricated in large high density arrays for simultaneous sensing operations. Since then, variants of the doubly clamped beams have been developed [43], including singly clamped beams [44], known as cantilevers, and membrane resonators [45].

MEMS resonators can sense the presence of analyte using static and dynamic testing methods. For most sensing applications, the analyte is required to attach to the

receptor layer that is deposited on the surface of the cantilever. Depending on the sensing application, the receptor layer can be tailored or functionalized. Sensing by static testing method monitors the cantilever bending due to the change in surface stress caused by the analyte attaching to the receptor layer. This method can be very sensitive. However this method requires large external equipment for high resolution and sensitivity detection [4]. The dynamic testing method monitors the change in resonant frequency caused by the change in mass of the resonator. The detection of resonant frequency shift can be extremely sensitive under ideal conditions, such as vacuum or ultra high vacuum, where the air dampening is minimal and the quality factor is at its maximum. Although the resonators can achieve sensitivity as high as attograms (10^{-15} g) [46], most sensing devices are expected to function in ambient air, where dampening and reduction of the Q factor occurs. A more practically achieved sensitivity is on the order of picograms (10^{-12} g) [47].

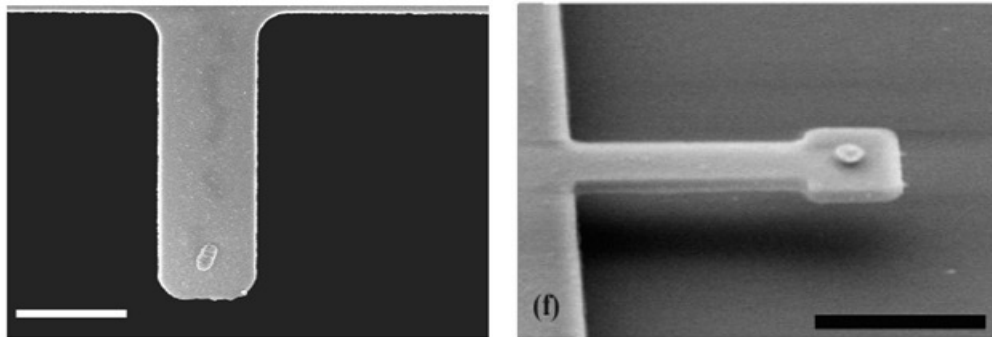


Figure 1.9 Cantilever sensor detection of (left) single E. Coli cell (600fg) and (right) chemisorptions of thiols on gold (0.39ag) [4]

While resonators in ambient air face dampening which decreases the sensitivity of the sensor, liquids incur larger dampening, which decreases the sensitivity further. As a result, there have only been a few demonstration of dynamic resonator sensing in liquid [7]. Recently, there have been demonstrations of resonator sensors

taking advantage of this dependence on the surrounding fluid to sense the viscosity by monitoring the change in resonant frequency and quality factor [49].

Some applications of resonator sensors include pressure [48], pH [49], temperature [50], and chemical and biological molecules [51] sensors. Typical resonator biosensors detect DNA [52], bacterial viruses [46], enzymes [53], cells [54], and pathogenic proteins [55], for diagnostic, prevention, and investigation applications. Limitations of this technology lie in the selectivity of the receptor layer and the sensitivity and resolution of the resonator's readout mechanism.

1.3. Device Readout

1.3.1. Overview

Resonator sensors require a displacement readout mechanism for both testing methods, as detailed in section 1.2.5 to determine the displacement of the resonator. The readout mechanism is often the limiting factor that determines the sensitivity of a sensor, which is based on its accuracy and the precision. There are many different readout mechanisms, including piezoresistive, piezoelectric, capacitive, and optical, each with their respective interfacing circuits [4].

1.3.2. Piezoresistive Readout

Piezoresistive readout mechanisms utilize the change in piezoresistive material resistance based on the applied mechanical stress. The change in resistance caused by resonator actuation can be straightforwardly monitored by resistor measurement circuits. A typical measurement circuit is the Wheatstone bridge [56], which utilizes three known resistances to measure the unknown resistance. A simple

form of piezoresistive material is doped silicon, with typical square resistance on the order of several hundred ohms. However, parasitic and electric noise and interference limits piezoresistive measurement sensitivity.

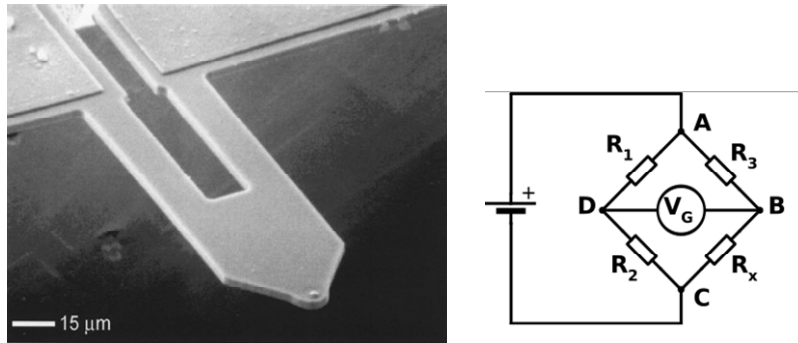


Figure 1.10 Schematic of a piezoresistive readout method and an interfacing Wheatstone Bridge circuit and micrograph showing a piezoresistive cantilever [4]

1.3.3. Piezoelectric Readout

Piezoelectric readout mechanisms utilize the change in electric potential across the piezoelectric material due to applied mechanical stress. This potential is seen across the stressed material due to the separation of charge across the crystal lattice [57]. The potential is read across an open-circuit and often amplified. Piezoelectric sensors are used in pressure sensors, typically microphones. This measurement technique suffers from the same drawbacks as piezoresistive readout.

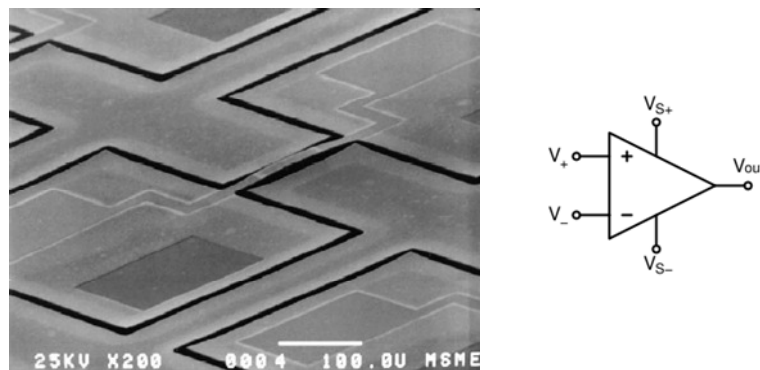


Figure 1.11 Schematic of a piezoelectric readout method and an interfacing differential amplifier circuit and micrograph showing a piezoelectric beam resonator [58]

1.3.4. Capacitive Readout

Capacitive readout is often used for resonators due to the simplicity of its implementation. This measurement scheme requires two conductive plates that are integrated into the device design. The resonator displacement causes a change in capacitance due to the change in distance between the parallel plate capacitors. The change in capacitance can be measured by very sensitive capacitance measurement circuits. Typical devices use current conveyors to collect the induced current due to changes in capacitance with respect to time. Capacitive readout has shown to be an effective technique, but still suffers from electric noise and parasitic capacitance effects. The gain of the current conveyor is also highly dependent on the parasitic layout of the circuit, influencing the spectral resolution of capacitance measurement [59].

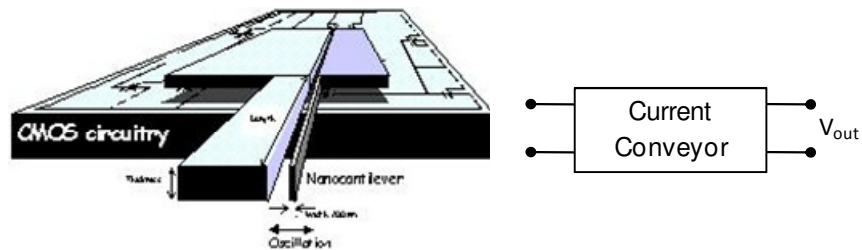


Figure 1.12 Schematic of a capacitive readout method and a possible interfacing circuit

1.3.5. Optical Readout

There are numerous optical readouts used in resonator sensing. One of the most sensitive readout method is shining a laser onto the surface of a cantilever and collecting the light reflected onto a position sensitive detector (PSD) [60]. This measurement method is employed in atomic force microscopy (AFM), possessing

high displacement measurement resolution. The measurement's main drawback is its requirement of large bulky external equipment that limits its application: (1) outside of a laboratory environment and (2) large resonator array integration. In addition, the stringent laser alignment accuracy onto the surface of the resonator limits the minimum resonator size, and potentially the sensitivity of a sensor.

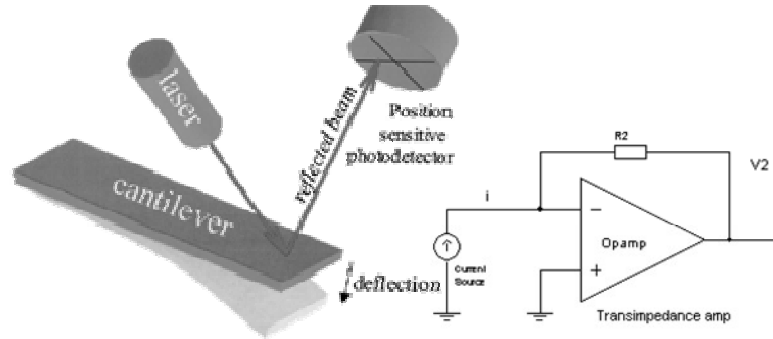


Figure 1.13 Schematic of an optical readout method and an interfacing transimpedance amplifier circuit

A second optical readout measurement is by interferometry [52], which utilizes the interference pattern of coherent light to measure displacement. By monitoring the interference patterns, ultra-sensitive displacement resolution can be achieved. Optical interferometry possesses similar limitations as AFM technique, requiring large and bulky external equipment found in a laboratory setting.

In plane optical coupling possesses the typical high resolution associated with optical readout method but eliminates the need for extensive free-space optical equipment. In plane optical coupling consists of a cantilever that doubles as an optical waveguide and a fixed output collector waveguide. By monitoring the coupling change across the air gap, the misalignment can be inferred and calculated. This measurement technique has been chosen for the experiments in this work and will be further described in Chapter 2 [14].

The interfacing circuit used by optical readout methods is a transimpedance amplifier that receives the current signal from the photodetector and produces a voltage output. Transimpedance amplifiers can be implemented using an operational amplifier and a resistor.

1.3.6. Feedback Circuit

The development of an interfacing circuit provides real-time displacement output which enables the development of feedback systems [10, 11]. Feedback systems are used to enhance the functionality of the system and at the same time eliminate the use of external equipment, allowing future system on-a-chip integration. Sensitivity enhancements [12] and autonomous resonant frequency tracking [13] are examples of enhancements demonstrated by the use of feedback systems.

There are many types of feedback circuits employed for the detection and tracking of the resonant frequencies. A universal feedback circuit design cannot be established due to the variation in resonator properties, designs, and functionalities. There are two popular designs implemented: (1) direct resonance oscillator (DRO) and (2) phase locked oscillator (PLO) [61].

The DRO design executes a self-excitation algorithm that utilizes the resonant displacement signal caused by ambient energy to drive the resonator at its resonant frequency by adjusting the actuation signal's gain and phase [8]. The DRO can be implemented multiple ways. A common design consists of connecting an amplifier to the interfacing circuit, then serially connecting a phase shifter before feeding the signal back to the resonator device as the actuation signal. One or multiple differential

operational amplifier(s) are used in the amplifier stage. A loaded-line phase shifter or an all-pass filter can be used as the phase shifter stage [11, 13, 62, 63].

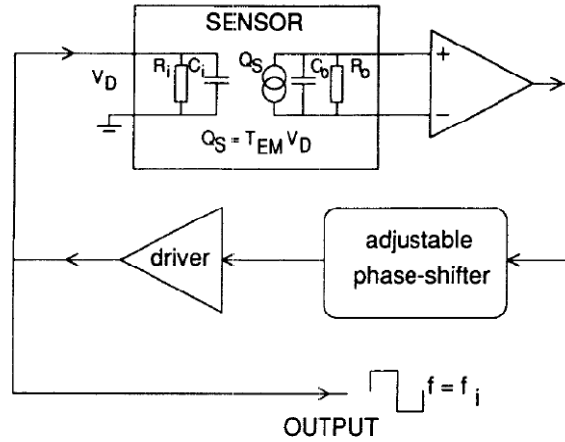


Figure 1.14 A block diagram showing the components of a DRO feedback system [62]

The PLL consists of a phase locked loop (PLL) and a phase shifter connected in series. PLL is a control system that generates a signal that has fixed phase relationship as a reference signal. The PLL circuit locks onto the frequency and phase of the reference signal, the resonator displacement signal in this case, and automatically changes the frequency of a controlled oscillator until the generated signal matches the reference signal. A PLL generally consists of a phase detector, low pass filter, and voltage controlled oscillator (VCO). The VCO generates a periodic signal based on a controlled voltage input obtained from the low pass filter. If the oscillatory signal falls behind the reference signal, the low pass filter receives an increase voltage from the phase detector, thus increasing the VCO's output frequency. Likewise, if the oscillator signal creeps ahead of the reference signal, the low pass filter obtains a signal from the phase detector to decrease the VCO's output frequency. The matched oscillatory signal is then phase shifted, similar to that of the DRO, and fed back to the resonator as the actuation signal.

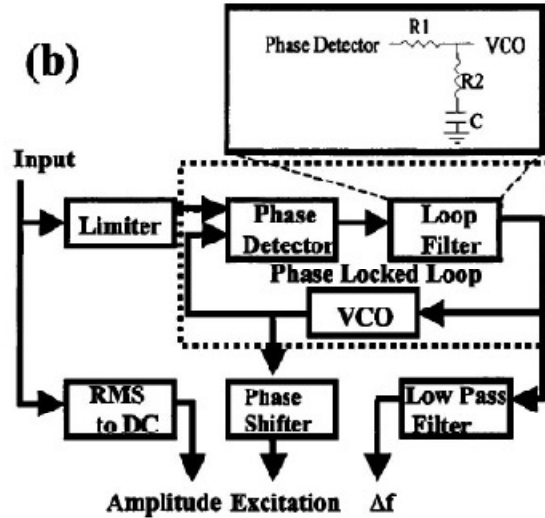


Figure 1.15 A block diagram showing the components of a PLO feedback system [61]

The main difference between DRO and PLO is that DRO utilizes the signal generated by the resonator itself to drive the resonator. Whereas, the PLO matches the signal generated by the resonator via a PLL and drives the resonator by the output signal of the PLL. The PLO provides an output signal, which feeds into the VCO to detect and track the resonant frequency of the resonator. A PLO system requires an additional component such as an external spectrum analyzer or on-chip frequency counter to determine resonant frequency.

Tailored amplitude and phase compensation stages are required for both feedback circuit designs since correct amplitude and phase relationship need to exist to sustain actuation at the resonant frequency. Since each device requires a unique circuit to be design, these feedback systems cannot be used universally for readout and control [8]. An adaptive feedback circuit that can accommodate a wide range of resonator designs and resonant frequencies would circumvent these constraints and establish a single feedback circuit for a large number of resonators.

1.3.7. Integration

MEMS devices and microelectronics can be integrated by monolithic integration or hybrid integration, with system in package (SIP) and system on chip (SOC) technologies, respectively. Monolithic integration combines MEMS devices with control electronics in the same fabrication and packaging process. Hybrid integration combines the two technologies, post-fabrication, in the same packaging process. Monolithic integration offers reduced parasitic capacitance, high reliability, high density, small device footprint, and increased performance, such as increased speed and reduced noise. Hybrid integration is used to integrate different substrate materials and incorporate incompatible fabrication processing steps. Cost can influence the method of integration used, as the cost of manufacturing can vary according to the method and approach used during fabrication and packaging.

(i) Monolithic Integration

There are three basic approaches to monolithic integration: “microelectronics first”, interleaved, and “microelectronics last”. “Microelectronics first” entails completing the fabrication of the microelectronics using standard CMOS technology first before the fabrication of the MEMS device. A passivation layer is deposited onto the microelectronic region to protect it during the MEMS fabrication procedure. To make electric connections to the circuit windows can be etched through the passivation layer or it can be stripped off completely. When using this approach, the high temperature processes used during MEMS fabrication need to be minimized to prevent damage to the CMOS components. Annealing for stress relief in thin films is

an example of a high temperature process which is above the melting point of aluminum interconnects. In addition, high temperature can also strongly affect the performance of CMOS devices due to further drive-in of dopings. Researchers have developed novel methods to overcome some of these challenges. Tungsten has been used to replace aluminum metallization in CMOS, withstanding subsequent high temperature processes [64]. Low temperature depositions, below 450°C, of thin films have also been recently developed in order to be compatible with conventional aluminum layers in CMOS technology [65].

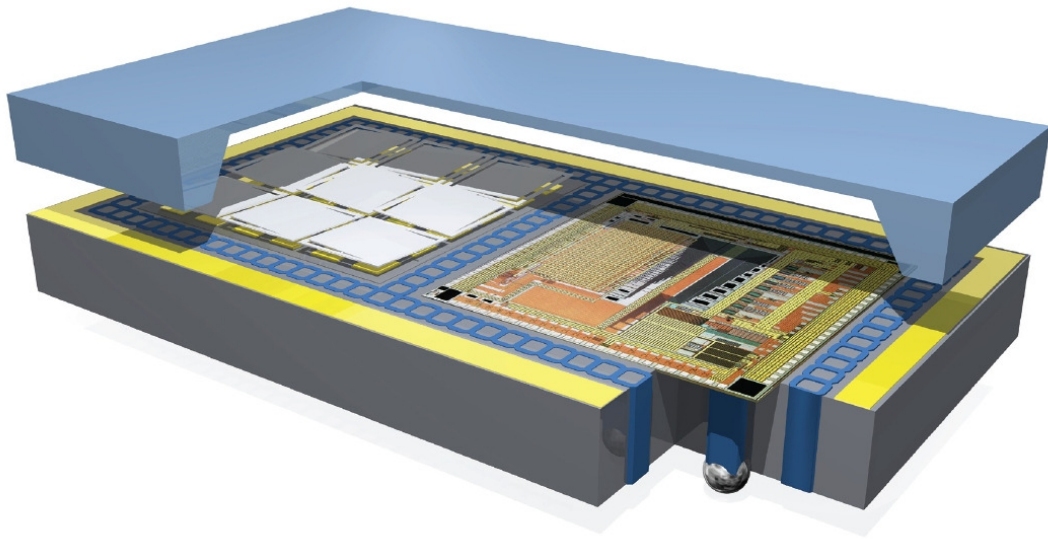


Figure 1.16 Schematic of a monolithically integrated system [66]

The interleaved approach tries to accommodate the fabrication processes of MEMS and microelectronics simultaneously. Interleaved approach is not suited for all designs, since the fabrication specification and process order is very stringent. The interleaved approach often requires many iterations of passivation deposition and removal to protect and expose different regions of the chip as the process interleaves between the two subsystems.

Sandia National Laboratories (SNL) introduced a third approach, “microelectronics last”, to prevent the negative effects on microelectronics due to MEMS fabrication steps [65]. All MEMS fabrication is completed first, followed by the microelectronics, eliminating all problems associated with high temperature annealing. This approach can be limited due to the non-planar structures caused by extrusions of the structures out of the wafer surface causes step coverage, stringers, the pooling of photoresist problems. To overcome this issue, SNL etched a shallow trench below the surface of the wafer. After the fabrication of microstructures in the trenches, sacrificial oxide was deposited in the trenches and then planarized using chemical-mechanical polishing (CMP). The wafer, with embedded microstructure, is now planar and ready for CMOS processing [64, 65].

(ii) Hybrid Integration

Even with the recent development of monolithic integration, there are still a number of situations that require the use of hybrid integration. For example, it is not feasible to integrate optoelectronics with microelectronics on the same substrate. In this case, multi-chip bonding is required during packaging. MEMS fabrication often requires CMOS incompatible materials that can contaminate critical processes. As a result, devices are required to be fabricated separately and assemble together post-processed. There are two methods of making interconnections between chips, wire bonding and flip chip bonding.

1.4. Thesis Organization

This thesis will be organized as follow. Chapter 1 gives a background for this research and establishes the motivation behind this project. The second chapter will

describe the design and functionality of a resonator. More specifically, an optical chemical sensor resonator, which will be used as the main platform to test and ultimately integrate with the feedback circuit, will be described in detail. The third chapter will present the design of the feedback circuit, starting from the optimization algorithm used and followed by its circuit implementation. PSPICE simulation of the circuit will be shown. Based on the simulation results, challenges and critical parameters will be presented. The fourth chapter will describe the testing of the feedback circuit. The experimental setup and two testing procedures are presented, followed by the results of the testing and its analysis. The fifth chapter will introduce and discuss electrospray deposition (ESD) processes and their characterization for use with MEMS fabrication. The final chapter, chapter six, will give a summary of the research presented in this thesis. Future work will be presented, followed by a brief analysis of the potential impact of this work and the final conclusion.

Chapter 2. Resonator

2.1. Introduction

A III-V resonator microsystem was chosen as a platform to test and characterize the development of the enhancements outlined in this thesis. The microsystem consists of a MEMS cantilever waveguide resonator sensing platform utilizing III-V Indium Phosphide (InP) as a substrate material. This cantilever waveguide resonator was chosen for its high sensitivity and ability to be integrated into a sensor microsystem. The cantilever sensor, actuated electrostatically, was first presented in [36].

2.2. Electrostatic Force

The electrostatic force produced by an applied voltage is analyzed here using a first-order model. The voltage is assumed to be applied to a capacitor formed by a capacitor plate and a parallel fixed structure. The two planes of the capacitor are assumed to be ideal plates with air dielectric in between. In this analysis, uniform and constant electric fields are assumed and fringing fields at the edges are ignored. The force is calculated for a static cantilever where the distance between the parallel plates is kept constant. The change in distance caused by the electrostatic force is ignored. The table below lists the variables involved in the analysis.

Table 2-1. Table of Variables I

Symbol	Definition
V	applied voltage
C	capacitance
Q	charge of capacitor
W	electrostatic potential energy stored in a capacitor
F	force between plates
y	distance between plates
A	area of plates
ϵ_0	dielectric permittivity of the capacitor

Equation 2-1 gives the accepted electrostatic potential energy stored in a capacitor given the capacitance and an applied voltage. The force between the capacitor plates can be derived from the spatial dependence of the potential energy given in Equation 2-2. dC/dy can be calculated from Equation 2-3, the capacitance of an ideal parallel plate capacitor with two parallel plains of area A, separated by a distance y. By using Equation 2-2 and Equation 2-1, the force between the capacitor plates can be estimated by Equation 2-4.

Equation 2-1

$$W(Q, y) = \frac{1}{2} CV^2 = \frac{Q^2}{2C}$$

Equation 2-2

$$F_y = \frac{dW(Q, y)}{dy} = \frac{Q^2}{2C^2} \frac{dC}{dy} = \frac{1}{2} V^2 \frac{dC}{dy}$$

Equation 2-3

$$C = \frac{A\epsilon_0}{y}$$

Equation 2-4

$$F_y = -\frac{dW(V, y)}{dy} = -\frac{V^2 A\epsilon_0}{2y^2}$$

2.3. Cantilever Beam Theory

The first order analysis of cantilever beam theory is presented here. The assumptions made in this analysis include: the length of the cantilever is much longer than its width and thickness, the bending of the cantilever is negligible compared to its dimension, and the clamped end of the cantilever is fixed. These assumptions simplify the calculation and enable a closed form solution. This first order analysis is only used to estimate the cantilever displacement and its resonant frequency to give an approximate range of cantilevers that the feedback circuit can operate with. Below is a list of variables used in the analysis with their definition.

Table 2-2 Table of Variables II

Symbol	Definition
L	cantilever length
H	cantilever thickness
W	cantilever width
I	Moment of Inertia
E	Young's Modulus
P	volume mass density
ν	Poisson's ratio
x	distance in the x-axis
w	displacement from the neutral axis
z	distance in the y-axis
P	force per unit area
ϵ	strain
k_{eff}	effective spring constant

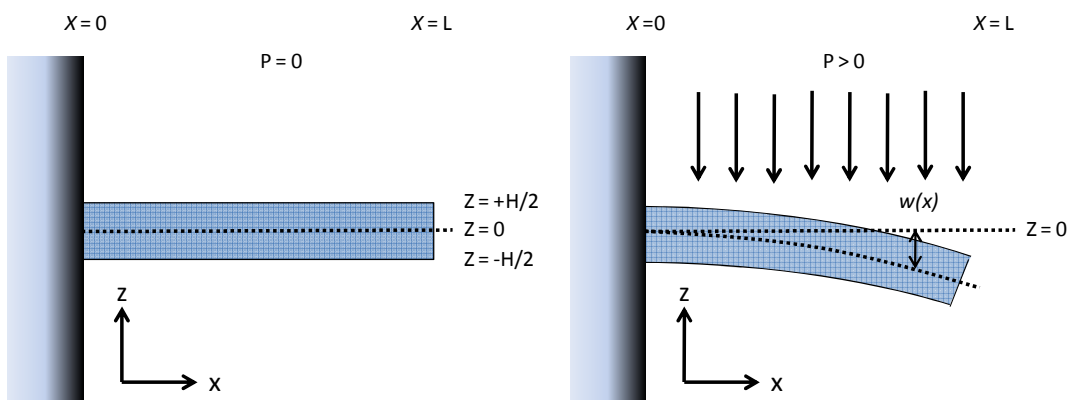


Figure 2.1 Diagram showing (left) beam position at no load condition and (right) beam bending in the z-direction at distributed load condition

According to Senturia [67], the bending of a cantilever beam can be expressed as Equation 2-5, assuming distributed load across the beam. Based on the previously stated assumptions, the boundary conditions of the beam are $w(0) = 0$ and $\frac{dw(0)}{dx} = 0$. Applying these conditions to Equation 2-5, the displacement along the x-direction can be given by Equation 2-6 for a given load P . I is the cantilever's moment of inertia about its neutral axis expressed as,

Equation 2-5

$$I = \frac{WH^3}{12}$$

The cantilever max displacement, at its tip ($x=L$), can be derived by substituting in L for x , and I (Equation 2-4) and P (Equation 2-4) into Equation 2-6. Using this expression, the maximum cantilever displacement of various geometries can be calculated, which will help determine the range of cantilevers suited for the feedback circuit.

Equation 2-6

$$\frac{d^4w}{dx^4} = \frac{P}{EI}$$

Equation 2-7

$$w(x) = \frac{PWL^2}{4EI}x^2 - \frac{PWL}{6EI}x^3 + \frac{PW}{24EI}x^4$$

Equation 2-8

$$w(L) = \frac{PWL^4}{8EI} = \frac{3\varepsilon_0V^2L^4}{4y^2EH^3}$$

Figure 2.2 shows the dependence of displacement with respect to the cantilever length. Displacement on the order of device dimension is not properly estimated since the model only assumes small displacements. Figure 2.1 also shows

the dependence of applied voltage, varying from 5V to 15V, voltage typically available in electronics.

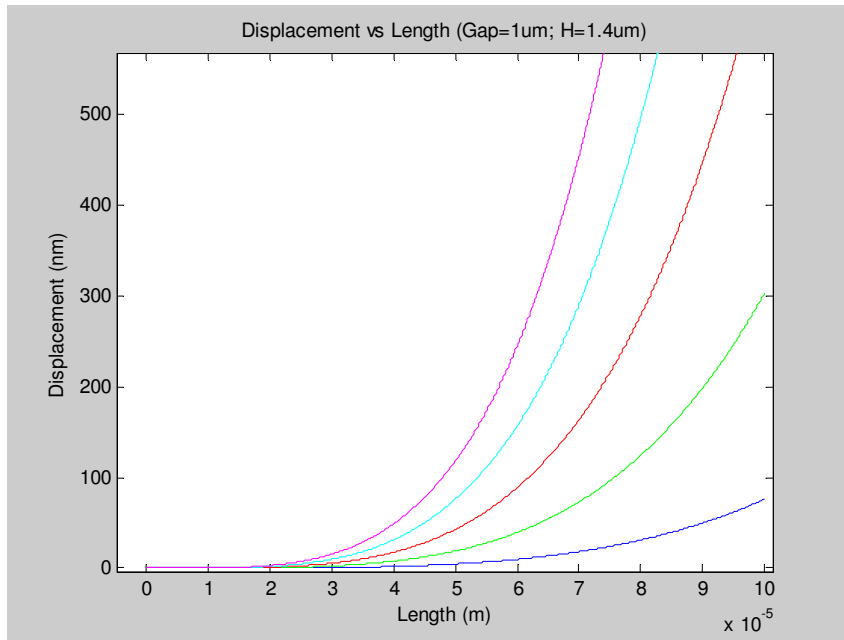


Figure 2.2 Graph showing relationship between cantilever length and tip displacement for an applied voltage of 26V.

If a single point on the beam was observed, the cantilever behaves like a linear spring, with a spring constant k_{eff} , expressed in Equation 2-7. If the displacement at the tip of the cantilever is considered ($x = L$), plug in Equation 2-6 into Equation 2-7 and solve for k_{eff} , we arrive at Equation 2-8, which will be useful to derive the resonant frequency of the cantilever

Equation 2-9

$$F = k_{eff}w(x)$$

Equation 2-10

$$k_{eff} = \frac{F}{w(L)} = \frac{PWL}{w(L)} = \frac{8EI}{L^3}$$

The resonant frequency of a standard lumped mass-spring system is $\omega_o = \sqrt{k/m}$, assuming there is no dampening. Lumped mass-spring system model

cannot be applied to a cantilever because the cantilever mass is distributed across the entire cantilever where each point along the cantilever is oscillating. To calculate the resonant frequency of a cantilever, the Rayleigh-Ritz method is used. The method is based on the fact that in oscillating system, energy is transferred periodically from elastic and kinetic energy. Thus, by setting the maximum kinetic energy to maximum elastic energy, the resonant frequency of the device can be found.

Kinetic energy of the cantilever can be calculated by integrating point kinetic energy over the entire volume, given in Equation 2-11. $w(x,t)$, the displacement of the cantilever from equilibrium at point x along the cantilever is given by $w(x,t)=w(t)\cos(\omega t)$ for harmonic oscillation. Using $w(x,t)$ in Equation 2-11 gives Equation 2-12. Similarly, elastic energy can be obtained from Equation 2-13, integrating point elastic energy over the entire cantilever volume, where

$\varepsilon(x, z) = -z \frac{d^2 w}{dx^2}$ is the point strain.

Equation 2-11

$$W_{k,\max} = \int_{\text{volume}} \frac{1}{2} \rho \left(\frac{\partial^2 w(x,t)}{\partial t^2} \right)^2 dx dy dz = \frac{\omega^2}{2} \int_{\text{volume}} \rho w(x)^2 dx dy dz$$

Equation 2-12

$$W_{e,\max} = \int_{\text{volume}} \frac{1}{2} E \varepsilon(x, z)^2 dx dy dz$$

By setting $W_{k,\max} = W_{e,\max}$ and utilizing Equation 2-7, cantilever's resonant frequency, ω_o , can be derived. The solution, given in Equation 2-13, can be solved analytically.

Equation 2-13

$$f_o = \frac{\omega}{2\pi} = \frac{9}{\sqrt{26}\pi} \sqrt{\frac{EI}{\rho HWL^4}} \approx 0.56 \sqrt{\frac{EI}{\rho HWL^4}}$$

2.4. *Optical Modeling*

The resonator sensor platform that the feedback circuit is controlling utilizes an in-plane optical readout that is discussed in Chapter 1. A schematic of the operation of optical coupling between the cantilever waveguide and the collector waveguide is shown below.

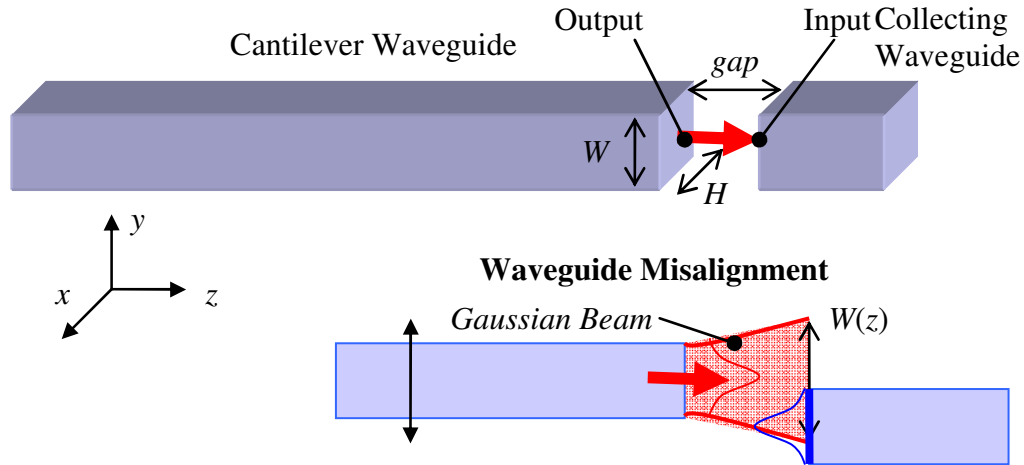


Figure 2.3 Schematic showing the optical coupling and waveguide misalignment between the cantilever waveguide and the collecting waveguide

The coupling across the gap is dependent on the gap distance and the misalignment of the cantilever waveguide. The misalignment can be due to residual stress caused by fabrication processes or by electrostatic actuation. The analysis below will estimate the percentage of coupling loss due to waveguide misalignment. This optical model will be calculated with the displacement analysis, derived in the previous section, to obtain a relationship between the coupling losses with applied voltage for a specific cantilever. The result will estimate the required applied voltage based on the sensitivity of the photodetector.

The optical coupling loss is obtained by calculating the optical overlap integrals, based on the assumption of free space Gaussian beam propagation in the axial (z) waveguide direction [68]. Although the optical waveguide were not specifically designed for single mode propagation, Gaussian beam is still assumed. The field of the input and output wave is given by the Gaussian beam equations (Equation 2-14 and 2-15) as a function of x , y , z .

Equation 2-14

$$\phi_{output}(x, y, z) = \left(\frac{2}{\pi}\right)^{1/4} \frac{1}{\sqrt{H(z)}\sqrt{W(z)}} e^{\frac{-y^2}{H(z)^2}} e^{\frac{-(x-x_0)^2}{W(z)^2}} e^{-i\left(nk^2 + \frac{nkx^2}{2R}\right)}$$

Equation 2-15

$$\phi_{input}(x, y, z) = \left(\frac{2}{\pi}\right)^{1/4} \frac{1}{\sqrt{H(z)}\sqrt{W(z)}} e^{\frac{-y^2}{H(z)^2}} e^{\frac{-x^2}{W(z)^2}} e^{-i\left(nk^2 + \frac{nkx^2}{2R}\right)}$$

Where $H(z)$ and $W(z)$ are the beam width in the x and y direction respectively as a function of propagation in the z -direction.

Equation 2-16

$$H(z) = h \left[1 + \left(\frac{2z}{nkh^2} \right)^2 \right]$$

Equation 2-17

$$W(z) = w \left[1 + \left(\frac{2z}{nkw^2} \right)^2 \right]$$

Equation 2-18

$$R(z) = z \left[1 + \left(\frac{nkz}{2z} \right)^2 \right]$$

Where h and w are the thickness and width of the cantilever, respectively, z is the air gap distance, and n and k are the refractive index of the cladding and the propagation constant, respectively. While the Gaussian beam of the output wave will be shifted by the misalignment in the x -direction, x_o , caused by electrostatic force, the Gaussian beam of the input wave will not have any shift because it is fixed. The z -dependent phase front curvature is given by Equation 2-18. The mode overlap formed between the cantilever waveguide and the collecting waveguide can be given by Equation 2-19 [68].

Equation 2-19

$$T = \left| \iint \phi_{output}(x, y, z) \phi_{input}(x, y, z) dx dy \right|^2$$

Equation 2-19 is calculated in MATLAB and its misalignment versus coupling loss is shown in Figure 2.4

Maximum tip displacement due to electrostatic actuation, $w(L)$, as define by Equation 2-8, can be plugged into Equation 2-19 as x_o , to determine the relationship between applied voltage and coupling loss, Figure 2.5.

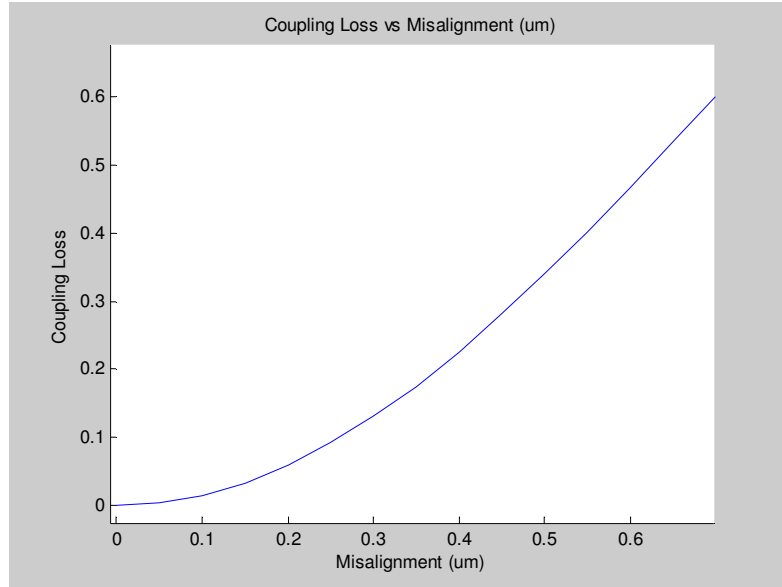


Figure 2.4 Graph showing the relationship between cantilever misalignment and coupling loss (L=50um, H=1.4um, W=1.2um, and Gap=0.6um)

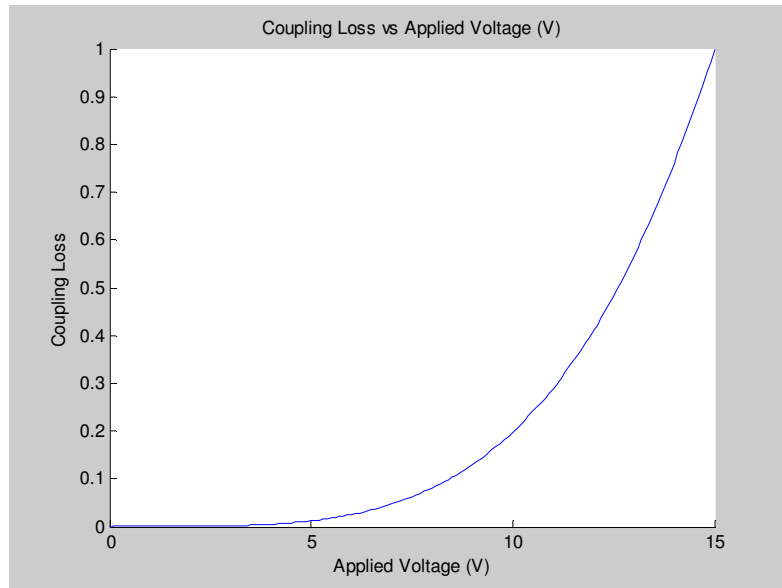


Figure 2.5 Graph showing the relationship between applied voltage and the coupling loss across the gap due to electrostatic displacement (L=50um, H=1.4um, W=1.2um, and Gap=0.6um)

2.5. Discussion

The result of the derivation and simulation shows the relationship between device dimensions and its resonant frequency. The calculated resonant frequency presented above does not accurately calculate the peak frequency of the cantilever

(the actual measureable resonant frequency), because the calculated resonant frequency does not take into account damping force such as air friction and energy dissipation in the cantilever material. The damping forces are difficult to solve analytically and are typically estimated empirically. The peak force, sometimes called the damped resonant frequency, is very similar to the calculated resonant frequency in practice. As a result, the calculated resonant frequency is taken as the theoretical resonant frequency in this work.

The analysis also revealed that there are physical limitations to the functionality of the resonators. Shorter cantilevers exhibit higher resonant frequencies and require higher forces to displace them. This places a limitation on the range of devices capable of integrating with any circuitry due to limited frequency response of components and available maximum voltage. The frequency response of the circuitry will limit the driving frequency, while the applied voltage will be limited by the circuit rails. Maximum actuation voltage will determine the maximum cantilever displacement. Minimum required displacement is dictated by the photodetector sensitivity. As a result, short cantilevers may be incompatible with the feedback circuit. The exact size limitation will be empirically determined since the sensitivity of the photodetector and noise of the system is too difficult to predict analytically.

Chapter 3. Feedback Circuit Design

3.1. Introduction

Circuit designers have developed CMOS circuitry for integration with microresonators, most often to achieve an on-chip system without the reliance on external instrumentation, enabling the entire system to be miniaturized, portable, and autonomous [5]. CMOS circuits have been shown to optimize the system by increasing resonator displacement read-out resolution [6], enhancing the quality (Q) factor of resonators [7, 8], and compensating for parasitic capacitive effects [5]. Detecting the natural frequency of a resonator is an integral part of their realization in cases such as to perform timing, to generate oscillation, and to sense analytes [9]. In addition, circuit integration can provide real-time outputs which enables the development of feedback systems [10, 11], enhancing the functionality of the system. This includes device sensitivity enhancements [12] and autonomous resonant frequency tracking [13].

3.2. Hill Climbing Algorithm

3.2.1. Concept

A hill climbing algorithm is a simple optimization technique that is used to locate the local extrema of a system. This algorithm is mostly used in computation and search algorithms [87, 88], targeting applications such as cost minimization [89], real-world modeling [90], and artificial intelligence [91].

The optimization technique is implemented in our design to locate the local maximum amplitude of the resonator system, through which the resonant frequency

of the resonator can be determined. Hill climbing maximizes (or minimizes) a function by locally sweeping the value of the function, comparing the present state to the past state until an extrema is located. If the present state is preferred over the past state, the direction of the local sweep remains the same. However, if the past state is preferred, the direction of sweep reverses (see Figure 3.1). More advanced optimization algorithms are available which perform similar function. However due to the simplicity of the resonator frequency response and the non-critical response time requirement, this simple algorithm is well suited for this application.

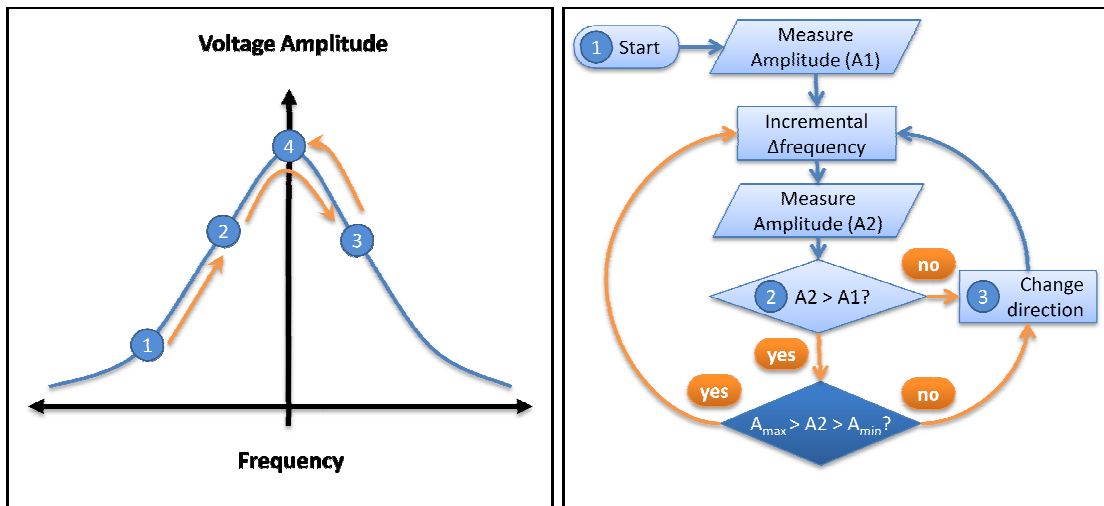


Figure 3.1 Diagram describing the hill climbing optimization algorithm used to locate the maximum amplitude at the resonant frequency.

The hill climbing algorithm sweeps a range of actuation frequency starting at a random point in a random direction. The algorithm will continue to sweep the frequency in the more favorable direction until maximum response is achieved at the resonant frequency, f_0 . Once f_0 is reached, a small steady state oscillation will occur as the algorithm sweeps around the optimal point, changing directions as it passes the apex. The small steady state oscillation around the resonant frequency is averaged (running average) to determine an estimate for the resonant frequency based on the

assumption that the averaged time period is much smaller than the time required to shift the resonant frequency.

3.2.2. Applications in MEMS

Optimization algorithms are seldom used in the field of MEMS for device operation, with most examples in design parameter optimization [92] and device calibration [93].

3.3. Circuit Implementation

3.3.1. Overview

The hill climbing algorithm is implemented using a four-stage feedback mixed-signal circuit, consisting of an amplitude detector, a differentiator, logic control, and a voltage controlled oscillator (VCO) stage, each of which will be further detailed in subsequent subsections. The resonator displacement signal is fed into the amplitude detector stage as the input of the feedback circuit. Completing the feedback is the VCO output that drives the resonator at a controlled actuation frequency (see Figure 3.2). The output signal to the system is taken at the VCO input bias voltage, which is correlated to the resonator driving frequency. At steady state, the drive frequency will be oscillating around the resonant frequency. The voltages in between each stage are labeled as they will be referred as $V1$ through $V5$ in the later sections.

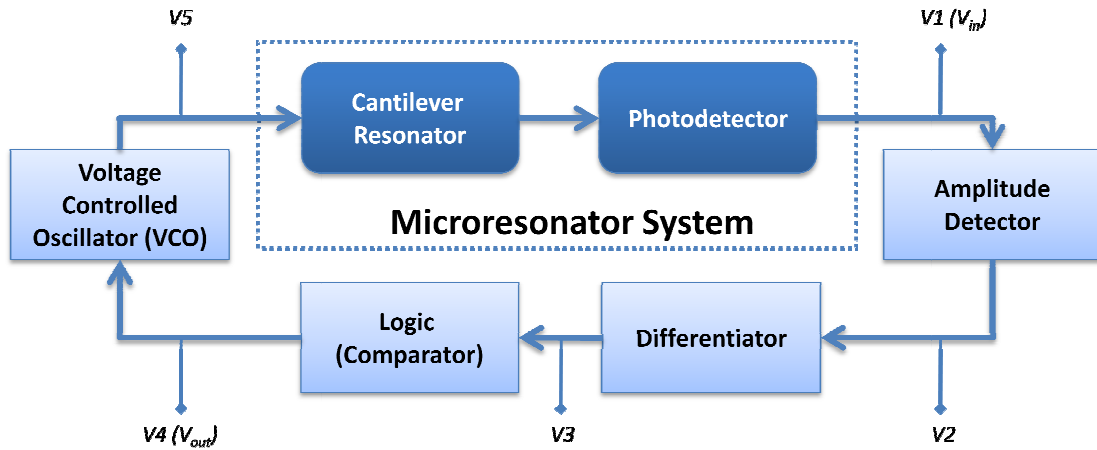


Figure 3.2 Feedback circuit diagram showing four-stage circuit integrated with chemical resonator sensor

3.3.2. Amplitude Detector

The amplitude detector stage is composed of a high-pass filter, an amplifier, a precision full-wave rectifier, and a low-pass filter. The displacement input signal, $V1$, of the resonator systems of interest ranges from 100 kHz to 1 MHz in frequency and exhibits millivolt amplitude, with a constant DC offset. To obtain the amplitude of the oscillating signal, $V1$ is first passed through a high-pass filter and amplified ($G=100$ V/V). The signal is rectified using a precision full-wave rectifier, which consists of summing two precision half-wave rectifiers, one of which is inverted and amplitude doubled, see Figure 3.3.

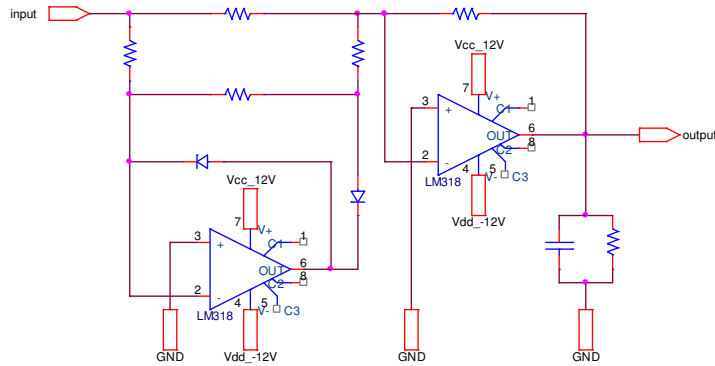


Figure 3.3. Circuit schematic of a precision full-wave rectifier built using two Op-Amps.

The precision rectifier is designed using generic components consisting of two high speed, low noise op-amps and diodes. The amplitude of V_I is obtained by capturing the envelope of the rectified signal using a simple RC low-pass filter. The RC value was determined using the estimate:

Equation 3-1

$$RC \sim \sqrt{1/\omega_r \omega_e}$$

where ω_r , ω_e are the frequency of the resonator and envelope, respectively. As ω_r varies by one order of magnitude and ω_e remains constant, the RC value remains within the same magnitude, still satisfying the used estimate. V2 will have an inevitable ripple on the order of 50 mV using this method.

3.3.3. Differentiator

The differentiator stage, which is composed of low-pass filters and a differentiator, determines the change in resonator signal with respect to time. A favorable and unfavorable change in response is defined as a positive and negative differentiation signal, respectively. The differentiation stage will cause an intrinsic gain in the frequency signal. Any high frequency ripple, resulting from the previous

envelop-detecting stage, will be amplified by orders of magnitude, drowning out any useful differentiated signal. Therefore, low-pass filters are applied to V_2 to maintain an acceptable signal to noise (S/N) ratio.

3.3.4. Logic Stage

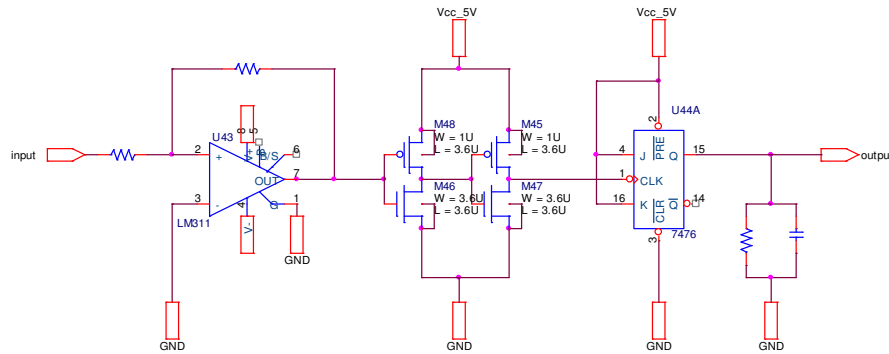


Figure 3.4. Circuit schematic of the logic stage comprising of a Schmitt Trigger, a T-FF wired from a J-K FF, and an RC integrator.

The logic stage determines the direction of sweep based on the change in response with respect to time, V_3 . This stage will trigger a change in direction when the differentiation signal changes from positive to negative, but maintain its direction for all other circumstances. This stage is comprised of a Schmitt Trigger, a Toggle Flip Flop (T-FF), and an integrator (see Figure 3.4). A Schmitt Trigger is a comparator with positive feedback which has a tunable threshold ($V_T = \pm(R_1/R_2)V_S$) that V_3 must achieve before the output is triggered. Utilizing the Schmitt Trigger provides greater noise immunity compared to that of a regular comparator which would cause rapid switching between high and low states due to signal noise.

The direction of the frequency sweep is based on the direction of signal change as determined by a T-FF, which changes state when the T input is held high and the clocked input is strobed, described by the characteristic equation

Equation 3-2

$$Q_{next} = T \oplus Q$$

If T is held high and the T-FF toggles on positive edge clock, the output toggles when the clock goes from low to high. When the Schmitt Trigger output is connected to the T-FF clock and low and high states correspond to negative and positive differential signal, the T-FF output will toggle when the signal response switches from positive to negative. Conversely, a negative change to a positive signal results in the output state remain unchanged. The output state of the T-FF determines the direction of the driving frequency sweep (high and low correspond to increase and decrease in driving frequency, respectively). An integrator is attached in series with the T-FF to integrate the digital signal, generating an input voltage bias, V_4 , serving as the VCO input and an output of the resonator feedback system.

3.3.5. Integrator

The integrator stage converts the digital signal from the logic stage into an analog signal that is fed into the VCO. The digital signal, withholding the information of direction of sweep, is integrated causing a decrease or increase in the VCO input bias dependent on whether the digital signal is high or low. The integrator used in simulation is an active integrator, with a linear integration coefficient of $-1/RC$.

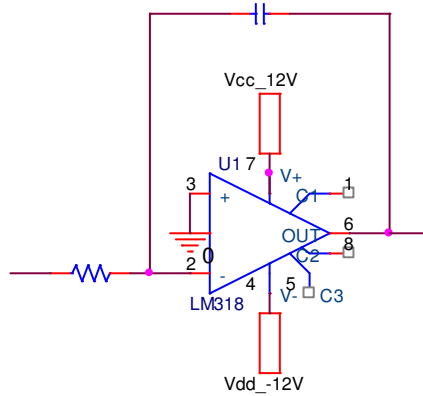


Figure 3.5 Circuit schematic of integrator

However, in actual implementation, a simple RC integrator was used instead. This is due to a larger signal noise level on the output of the active integrator compared to that of the passive integrator. Because the output frequency of the VCO will vary directly with the output of the integrator, the noise level should be kept at a minimum to decrease the frequency swing of the VCO. As a result, decreasing the noise level has the priority over the linearity of the integration. The linearity of the integration will ensure that the rate of increase towards the peak is the same as the rate of decrease away from the peak. Although linearity is preferred, the equal rate of increase or decrease is not a requisite for the hill climbing algorithm.

3.3.6. Voltage Controlled Oscillator

The VCO stage is the driving stage of the resonator feedback system. VCO output V_5 , is an oscillating signal whose frequency is dependent on an input voltage bias, V_4 . The output waveform is a square wave from 0 to 5 V, whose output frequency range can be tuned by biasing resistors and capacitors. Further signal processing can be performed on V_5 following the VCO output if required for driving the resonator, such as signal amplification.

By sweeping the V_4 , the frequency response of any resonator in the tuned range can be obtained. If the VCO is oscillating around the resonator's maximum response, f_o , the resonant frequency can be inferred by monitoring the VCO's mean input bias.

3.4. PSPICE Simulation

Initial simulation results showed high noise levels, signal distortion, and high current draw. Active low-pass filters were added to eliminate the main source of noise due to the differentiation of ripple noise. The V_T of the Schmitt Trigger was raised to reduce the impact of signal noise but as a result, caused a delay in signal propagation due to the extended time required to achieve the threshold level.

Signal distortion was also caused by interference between stages caused by loading effects. Op amp buffer stages were added between each stage to eliminate this distortion. High current draw was observed in the digital stage due to slow rise and fall time, $T_r = 8.8 \mu s$ and $T_f = 7.6 \mu s$, of the Schmitt Trigger output that was connected to the T-FF. The addition of two inverters to pull the signal to rail faster caused a decrease of T_r and T_f to 26.8 ns and 21.2 ns, decreasing the total current draw.

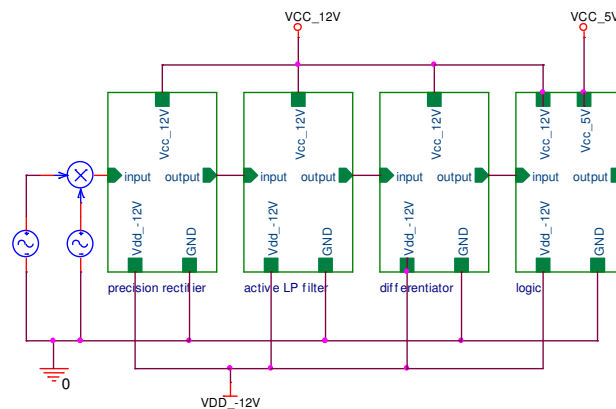


Figure 3.6. Hierarchical schematic of the open-loop circuit simulated in PSPICE where the

input signal was simulated using amplitude modulated signal

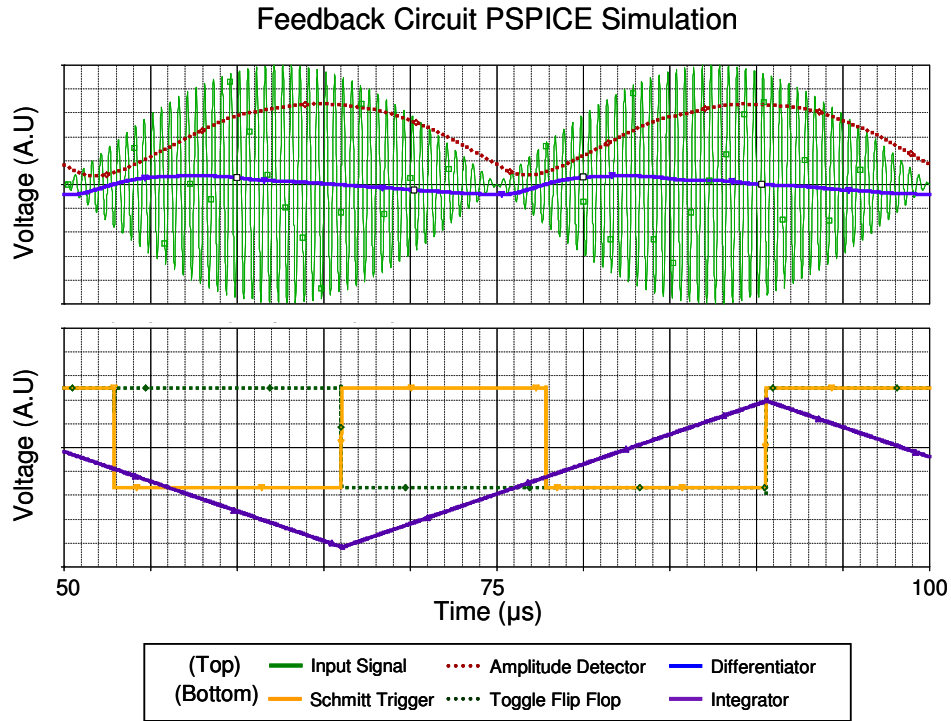


Figure 3.7. PSPICE simulation result showing output at every stage of the feedback circuit

The final simulation results, shown in Figure 3.7, demonstrate the successful implementation of the open-loop circuit, showing the output at each stage. The expected operation of each stage was investigated. The simulation output, at V_4 , switched sweeping direction when the amplitude changed from increasing to decreasing, but retained the direction of sweep when the amplitude changed from decreasing to increasing. A delay time of 10 μsec was calculated between V_4 and V_1 . μsec delay times are acceptable for the designed application, but should be minimized as much as possible to decrease oscillation amplitude around the f_o . This issue will be further discussed in the following sections.

3.5. Discussion

The feedback circuit was designed to autonomously operate a resonator sensor, detecting and tracking its resonant frequency. The difference between the hill climbing algorithm and existing algorithms is the independence of its driving signal from the frequency or phase of the displacement signal. Because only amplitude of the displacement signal is taken into account and no correlation in phase is needed between the input displacement signal and output actuation signal, a tailored phase compensation stage is not required. This eliminates the need of a separate design for each resonator and enables a universal feedback circuit for all resonators. The frequency sweep allows the feedback circuit to adapt to any peak within the sweep range.

The limitation of the hill climbing algorithm is solely due to the circuit implementation of the algorithm. Due to the non-ideal electrical components, they induce time delay, frequency cut off, distortion and loss of signal. As a result, a reduced device range can be operated, and they will exhibit decreased sensitivity. Under noiseless condition, a comparator ($V_T = 0V$) can be used to replace the Schmitt Trigger, which is needed for this practical case for greater stability under noisy conditions. Using a comparator will further reduce the propagation time delay and provide smaller amplitude of oscillation around the peak.

The PSPICE simulation of the open-loop circuit confirmed the implementation of the hill climbing algorithm by locating the maximum amplitude of the input signal. The direction of the frequency sweep changes when the maximum signal amplitude is detected.

As a general optimization algorithm, the input signal to this feedback circuit is not restricted to be the displacement signal of a resonator, nor is the algorithm limited to the detection and tracking of a resonant frequency. This hill climbing algorithm feedback circuit implementation can be applied to be used in any application that requires similar optimization.

Chapter 4. Detection of Cantilever Resonant Frequency

4.1. Overview

The circuit implementation of the hill climbing algorithm was constructed on a circuit board and utilized on a III-V optical resonator (optical resonator, see chapter 2) to detect its resonant frequency. The optical resonator was designed for chemical vapor sensing, but it was solely used as a resonator platform to perform and verify the detection of cantilever resonant frequency by implementing a hill climbing algorithm.

To verify PSPICE simulations and the implementation of the algorithm, an open loop circuit was first tested. The open-loop setup consisted of a function generator signal, V_{fg} , sweeping the input bias of the VCO at V_4 . By sweeping the input bias, the VCO output provided a square wave actuation, with a signal frequency spanning a range determined by the amplitude of V_{fg} . The VCO output signal drove the resonator, which provided a time variant optical coupling. The photodetector then provided the displacement response of the resonator, V_I , at the input of the amplitude detector, where the signal was then propagated through the algorithm. The open-loop output signal was readout at the output of the logic stage, which was disconnected from the input bias of the VCO. By sweeping a range of actuation frequency, the resonant frequency could be detected by monitoring the bias point that produced the peak cantilever amplitude response. To autonomously detect and lock onto its resonant frequency, a close-loop circuit implementation was required.

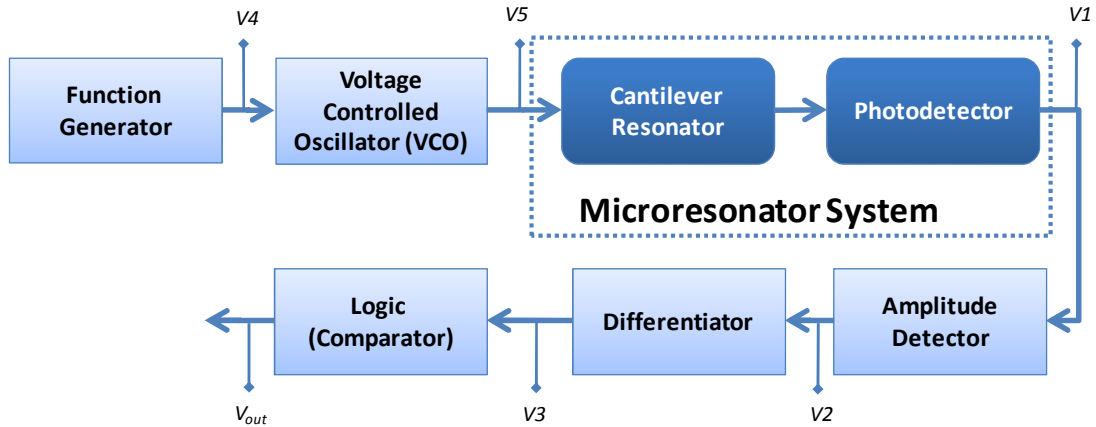


Figure 4.1 Block diagram of open-loop testing with the microresonator system

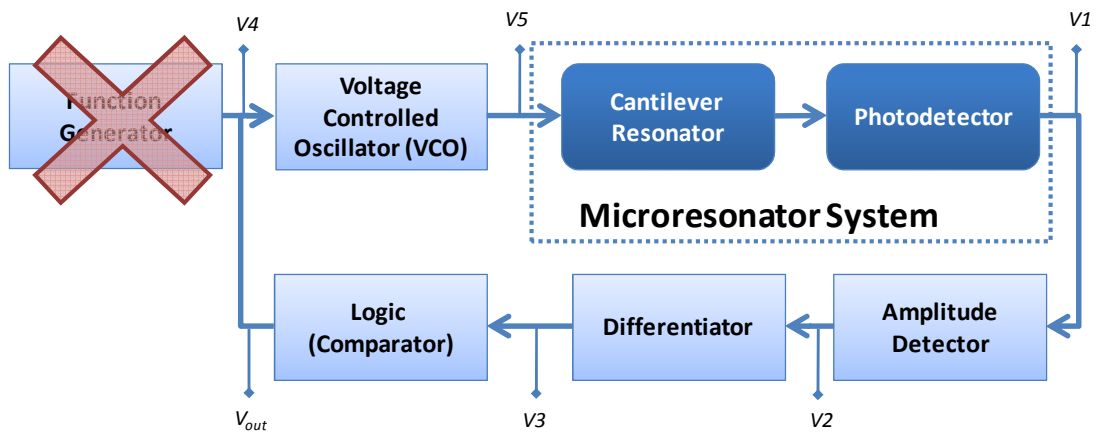


Figure 4.2 Block diagram of closed-loop testing after eliminating the function generator and connecting V_{out} to $V4$

To close the feedback loop, the function generator was disconnected and the output of the logic stage, V_{out} , was connected to the input of the VCO, $V4$. The closed-loop setup consisted of only the feedback circuit and the resonator. The output of the system was still taken at the output of the logic stage, $V4$, which should have been oscillating with small amplitude around the VCO input bias value, corresponding to the cantilever's resonant frequency.

4.2. Circuit Board Construction

The feedback circuit was built using discrete IC components on a circuit board, powered by ± 12 V analog and 5 V digital rails. A list of electrical components used to build the feedback circuit is listed in Table 4-1:

Table 4-1. List of Electrical Components Used

Component	Value
Op Amp	LM318
Diode	D1N914
T-FF	CD74HCT109E
Inverters	SN74LS04N
VCO	CD74HC7046AE

All electronic components were purchased from Digikey Corp.

Ideally, the feedback circuit should be implemented on chip and hybrid integrated to decrease parasitic effects and noise interference. However, because this demonstration is solely for the purpose of proof of concept, the circuit has only been built on a circuit board. By designing this circuit on a PCB board or fabricating it on chip, it is expected that the noise level and delay time should decrease and thus increase the resolution of the feedback circuit.

4.3. Experimental Setup

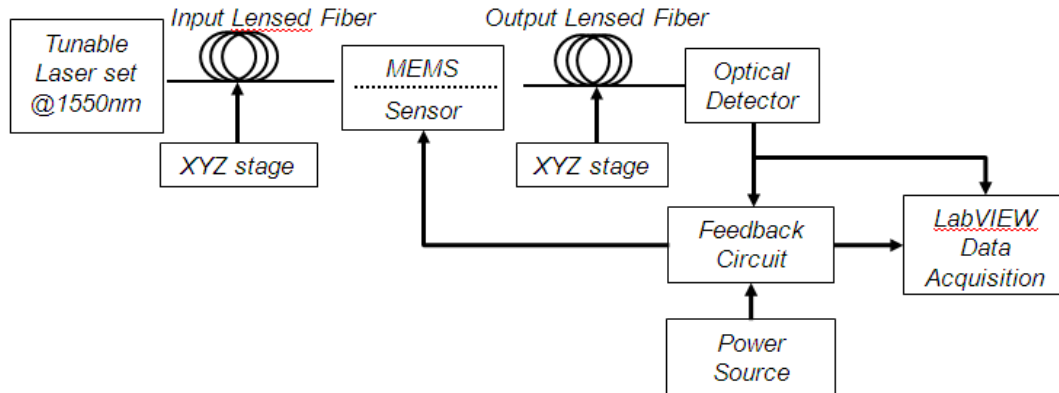


Figure 4.3 Diagram of experimental setup

Figure 4.3 is a diagram of the experimental setup. The optical resonator was operated by coupling light at 1550 nm wavelength from a tunable laser source (New Focus Venturi™ Tunable Laser 1520-1620 nm) into the device using a lensed fiber to focus the beam onto the waveguide input facet. A second lensed fiber collected light from the output waveguide facet which is then measured with a high speed photoreceiver (New Focus Model 11811 IR DC-125 MHz Low noise photodetector). Both lensed fibers have a focus spot size of 3.5 μm and a focal length of about 20 μm . The analog photodetector output signal is connected to the input of amplitude detector of the feedback circuit, V1. The output of the VCO circuit, V5, is applied to the resonator as the actuation voltage. A LabVIEW program was designed to log the input bias of the VCO, V4, and the optical coupling with respect to time. The data were imported into Microsoft Excel where it was analyzed.

During testing, 10-minute data sets were conducted. Acquisition of VCO input bias and photodetector coupling strength were recorded with a sampling frequency of 2 kHz. Based on Equation 2-13, expected resonant frequencies should range from 2.8

MHz to 63.6 kHz for these device lengths, respectively. The biased VCO has a resolution of 4.4 mV/kHz from 198 kHz to 971.3 kHz with 1.1 to 4.5 V input and R_{Bias} and C_{Bias} of 152 k Ω and 50 pF, respectively.

4.4. Open Loop Circuit

Open-loop design was first tested to verify the PSPICE simulation results. By sweeping the input signal, $V4$, at 1 Hz, the amplitude detector stage observed the frequency response of the cantilever within the sweeping range. The open-loop frequency scan of DeviceA ($W=1.4 \mu\text{m}$, $L=55 \mu\text{m}$, $T=1.8 \mu\text{m}$) showed a maximum amplitude at $V = 1.72 \text{ V}$, corresponding to a resonant frequency of 314 kHz. An asymmetric resonant frequency peak was observed. This effect was made more apparent by observing the amplified differential signal, $V3$. The divergence slope of the peak before f_0 has a maximum slope of 800 mV and a rise time of 75 ms and convergence slope has a maximum slope of -300 mV and a fall time of 100 ms.

High noise level was an initial concern during testing, causing increased circuit instability. The S/N ratio of the differential signal could be reduced by low-pass filtering, but the signal peaks would be then be distorted. By increasing the threshold level of the Schmitt Trigger instead, the logic stage properly determined the frequency sweep direction, matching the simulation results. However, a delay of 30 ms was observed at the output. This open-loop integration of the feedback system with the resonator cantilever demonstrated that it was feasible to locate the resonant frequency by utilizing the hill climbing algorithm. To autonomously locate and track the resonant frequency of the resonator, closed-loop feedback was required.

4.5. Closed Loop Circuit

The closed-loop system was completed by connecting the output signal of the logic stage to the input of the VCO, eliminating the simulated VCO input signal provided by the function generator. The initial VCO input bias was determined by the initial charge stored on the integrator capacitor in the previous stage, which was controlled by a potentiometer. After the initial turn-on, the small signal regulated the charge across the capacitor, insulating any DC voltage set by the potentiometer seen across the capacitor during the later transient and steady state stages. The transient and steady state stages are defined here as the operation period before and after feedback system has locked onto the resonant frequency of the device.

The transient stage frequency sweep exhibited a typical RC time constant as the integrator capacitor charged and discharged. The direction of the sweep, charging or discharging of the capacitor, was random since the initial state of the T-FF was random. If the direction of the initial sweep failed to locate a peak in response, the integrator would hit a voltage rail until the T-FF was toggled to change the direction of the sweep. As the resonant frequency peak was approached, the amplitude detector signal increased, creating a positive differential signal. The change from a positive to negative differential signal marked the apex of the peak. Due to the high Q of the peak, the dramatic decrease in amplitude triggered the Schmitt Trigger as it surpassed V_T , toggling the VCO to be swept back towards the apex, f_o . Operating in steady state, the feedback circuit oscillated around f_o , the apex of the resonant frequency peak. The direction of sweep continuously oscillated towards the direction of f_o , and as a result the signal was locked onto the resonant frequency, Figure 4.4.

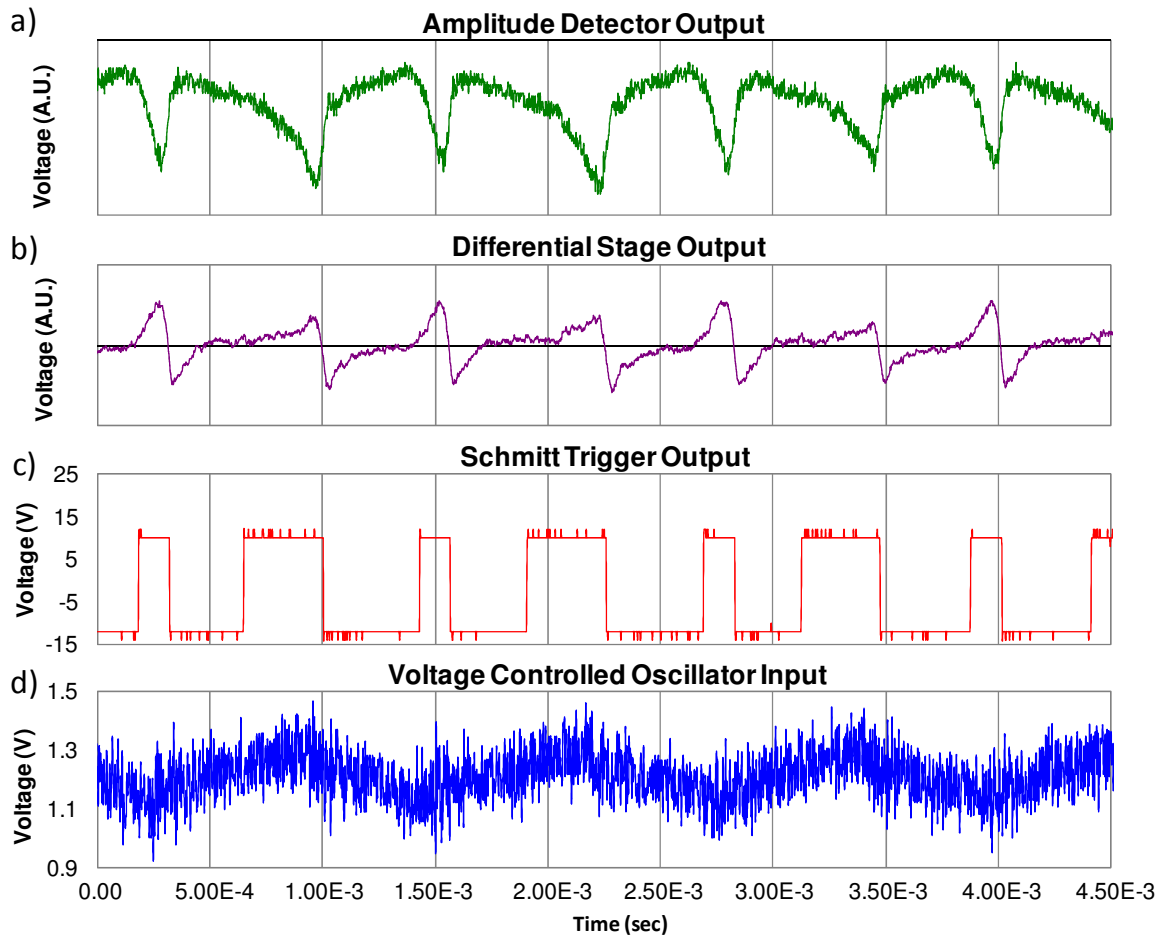


Figure 4.4. Output of individual stages of the feedback circuit while locked on to the resonant frequency. (a) Output of amplitude detector showing periodic peak amplitude, (b) differential signal of the amplitude detector, (c) Schmitt trigger output detecting the direction of the slope and (d) input of the VCO showing oscillation around a bias voltage

DeviceA ($W=1.4 \mu\text{m}$, $L=55 \mu\text{m}$, $T=1.8 \mu\text{m}$) had a mean input VCO bias of 1.721 V, which corresponded to a frequency of 314.0 kHz, a percent error of 1.54% compared to its theoretical resonant frequency of 309.3 kHz. The oscillation frequency around f_0 was approximately 800 Hz with an amplitude of 21 mV. The standard deviation of the input VCO bias' running average was 0.16 mV, corresponding to a frequency of 29.7 Hz.

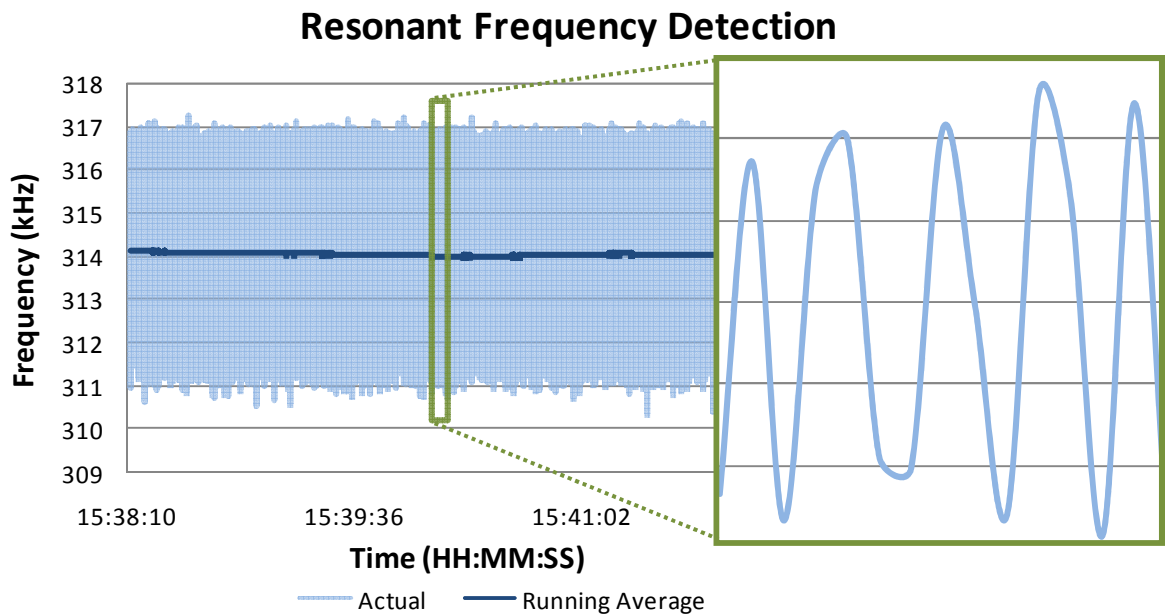


Figure 4.5. Showing a steady state signal around the resonant frequency (314kHz) of a $L=55\mu\text{m}$ $W=1.4\mu\text{m}$ and $T=1.8\mu\text{m}$ cantilever. The zoomed in graph shows the oscillatory signal around the resonant frequency, which could be calculated by applying a running average.

Six devices ranging in length from $40\ \mu\text{m}$ to $75\ \mu\text{m}$ ($W=1.4\ \mu\text{m}$, $T=1.8\ \mu\text{m}$), were tested with the same feedback circuit, resulting in the lock on their respective resonant frequencies ranging from $592\ \text{kHz}$ to $201\ \text{kHz}$, respectively. The minimum time averaged standard deviation of the set was $11.8\ \text{Hz}$ for DeviceB ($W=1.4\ \mu\text{m}$, $L=75\ \mu\text{m}$, $T=1.8\ \mu\text{m}$). Based on this minimum detectable frequency shift, the mass sensitivity of the system was $123\ \text{fg}$. The maximum time averaged standard deviation of these devices was $362\ \text{Hz}$.

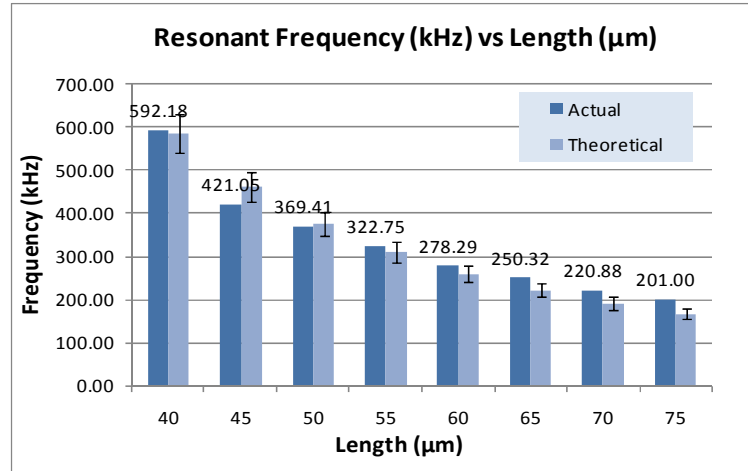


Figure 4.6. Resonant frequency detection of cantilevers ranging from L=40um to 75um together with their theoretical resonant frequency. Error bar for the theoretical values is based on 0.1um fabrication tolerance.

Resonant frequency was repeatedly locked onto using the feedback circuit. The difference of the time-averaged resonant frequencies between trial runs was within the stated standard deviation. Up to 60-minute long data sets were obtained with no signs of failure or deviation from the 10-minute scans. During the scans, there were occasions when the circuit lost track of the resonant frequency, resetting the feedback circuit to the initial transient stage, where the circuit was required to find and lock onto the f_0 again. The time required to relocate the f_0 appeared to be based upon the time required to toggle the T-FF to reverse the sweep direction, normally less than a millisecond.

Device lengths outside of the 40 μm to 75 μm range were tested. However, steady state operation was not consistently achieved. The VCO input bias was continuously swept, with no steady lock onto a constant voltage. The feedback circuit remained in the initial transient stage of the algorithm during the entire testing period.

4.6. Discussion

Theoretically, with ideal resonators and circuit optimization, this implementation of a hill climbing algorithm is capable of detecting the resonant frequency of any resonator. However, due to limitations of this resonator design, noise interference in the system, and frequency response of the IC components, this feedback system was limited to a subset of devices. The upper bound of cantilever length was 75 μm due to the limited optical coupling through the device. Longer cantilevers exhibited a greater out-of-plane curvature due to film stress, causing loss in optical coupling and resulting in a decreased S/N ratio below an acceptable threshold. As a result, the output frequency swept from rail to rail when testing devices above this length without ever establishing a consistent steady state.

The lower bound of cantilever length was limited by the frequency response and the supply rail of the electronics. As the cantilever length decreased, the cantilever f_0 increased and the required actuation voltage increased due to increased device stiffness, see Chapter 2. The increase in actuation voltage to displace the cantilever required a large bandwidth amplifier following the VCO output. As the driving frequency approached MHz, the actuation signal became distorted. This distortion limited the operation of the feedback circuit to devices with lower resonant frequency. This effect is not inherent to the algorithm, but to the resonator and circuit implementation components.

Resonant frequencies detected using the feedback circuit agreed with theoretical calculations within error and were independently verified using external equipment methods detailed in [14]. The measured and theoretical resonant frequency

discrepancies can be attributed to fabrication imperfections, which changes the f_o of a cantilever by as much as ± 2.2 kHz for DeviceA ($W=1.4 \mu\text{m}$, $L=55 \mu\text{m}$, $T=1.8 \mu\text{m}$), assuming $0.1 \mu\text{m}$ fabrication error. The amplitude of the oscillating signal around f_o was consistent during the 10 minute baseline measurement for the majority of the trials. However, some trials showed a change in amplitude of oscillation, which was attributed to a drift in optical coupling in the resonator setup. A mechanical drift in optical fiber alignment could have caused a decrease in optical coupling which led to a decrease in displacement signal strength. The weaker signal causes an increase in time required to surpass the V_T of the Schmitt Trigger, which resulted in larger amplitude of oscillation around f_o . This effect was observed in the testing of DeviceC ($W=1.4 \mu\text{m}$, $L=65 \mu\text{m}$, $T=1.8 \mu\text{m}$), where an approximate 5 mV increase in amplitude corresponded to a drift in coupling of 9 %. If the resonator setup can eliminate this drift and increase the displacement signal S/N ratio, the standard deviation of the feedback system output could be minimized and thus increase the overall sensitivity. A solution would be to implement an integrated on chip optical source and detector to increase coupling efficiency and eliminate the drift in optical coupling caused by the external setup.

Another limitation observed during testing was the failure of the feedback loop to lock onto the f_o of a resonator that exhibited two resonant frequency peaks that were within 100 kHz of each other. DeviceD ($W=1.4 \mu\text{m}$, $L=60 \mu\text{m}$, $T=1.8 \mu\text{m}$) was used as test device that had two superimposed resonant frequencies, 224.2 kHz and 329.0 kHz. The two resonant frequency peaks originated from the out-of-plane bending that caused a lateral as well as an out-of-plane actuation. Due to the

rectangular cross-section, the cantilever's in-plane resonant frequency was 81.9 kHz lower than its out of plane resonant frequency, which is a possible explanation for causing a superposition of two resonant frequency peaks. The feedback circuit experienced difficulty locking on to one peak because of the proximity to the second peak. The delay, caused by the elevated V_T , enabled the circuit to reach the second peak before it had a chance to toggle and return to the first peak. As a result, the hill climbing algorithm failed when the circuit did not recognize the trough between the peaks due to their overlap. This problem could be solved by reducing the V_T of the Schmitt Trigger, and thus the delay, enabling a faster toggle after the peak, before entering the trough. This limitation was not overcome in this work because the reduced V_T required higher signal to noise ratio than what was obtainable with the setup used.

Chapter 5. Electrospray Deposition

5.1. Introduction

The deposition of a polymer on the cantilever surface is the final step to creating viable sensors, providing the functionality needed for these devices to absorb desired analytes. Chemical sensors use a plethora of selective coatings from polymers to self assembled monolayers (SAMs) [4, 69, 70] to attract chemical species to the active areas of the devices. The vast majority of these coatings are a passive component of the sensor as a whole: a mass absorption or surface stress change is only measured from these layers by the appropriate transducer, and from these effects the chemical is inferred. To perform the sensing of multiple chemicals in parallel, multiple sensitive layers are usually required; complicating some of the common fabrication techniques.

Self assembled monolayers (SAMs) are a very common coating to create a functional surface for chemical and biological sensors [4, 71, 72]. The high quality of these films and their flexibility to be used in a variety of situations has made them a popular choice for chemical coatings. Their sensing mechanisms of these films are limited to surface sorption effects, which can be tailored for very specific chemical or biological attachments, but are poor in volumetric absorption.

Polymers such as polyethereurethane (PEUT), polyimide, or polycarbosilane [63, 73, 74] are also used as chemical sensing layers. These layers operate based upon absorption that increases mass, volume, or surface stresses depending on the transducer sensing function desired and the specific analyte/absorbing layer combination. Many polymers can be modified in such a way to increase affinity for

various chemicals, but due to various chemical properties (hydrophilicity, polarity, porosity, etc.) they do not always maintain the same type of extremely specific chemical affinities that SAMs provide. SAM coatings also present a greater level of patternability compared to these polymer layers which must often be spin-cast from a solution, or deposited using ink-jet printing techniques [75].

While a number of coatings are found in literature, the most robust of these layers are often found in the polymer coatings [76, 77]. Polymers are simple to work with, however a number of compatibility issues exist with the current fabrication process of the cantilever waveguides which requires the absorbing layers to be deposited after the complete fabrication of the sensor platform. This includes the completion of the wet release of the cantilever (H_2SO_4 and H_2O_2) and critical point drying (Alcohol) step. Due to the delicate cantilevers and waveguides and micron / sub-micron device dimensions, both solution immersion and ink-jet printing methods are not feasible; immersion because of stiction occurrence and inkjet printing for the large inkjet droplet size. One solution for the application of these layers is a deposition method called Electrospray Deposition (ESD) that is capable of thin film deposition for post process fabrication. ESD would circumvent problem of stiction for sub-micron release structures due to its ultra small aerosol droplet (diameter<50nm).

5.2. Concept

5.2.1. Overview

Electrospraying is a liquid atomization method by electrical forces often used for mass spectrometry and colloid thruster applications. By charging up a droplet to a

fraction of the Rayleigh limit, the magnitude of the charge on a drop exceeds the surface tension force, leading to the fission of the droplet. Droplets obtained using this method is extremely small, in some special cases down to nanometers in diameter. An electro spraying system is very simple, consisting mainly for a metal capillary and a high voltage (HV) source. It is a very versatile deposition process that is capable of depositing materials soluble in polar solutions. The main shortcoming of electro spraying, limited use in industry, is its low throughput. However, some proposed solutions include multi-nozzle, slit-nozzle systems, or mechanical spraying by rotary atomizers [78].

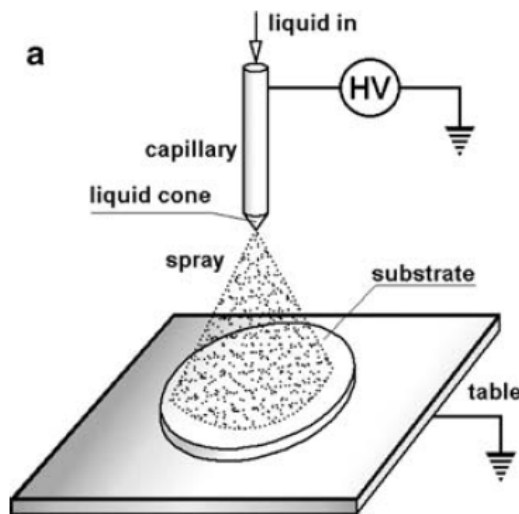


Figure 5.1 Diagram of electro spray deposition setup

The electro spraying process can be divided into four sub-processes that will influence the deposited film properties: (1) the cone-jet system and the factors that control its stability, (2) jet break-up and the resulting droplet size, (3) droplet evolution, and (4) deposition and film formation. A list of contributing parameters for each sub-process is summarized in Table 5-1. Because each sub-process is

interdependent, many parameters overlap and affect multiple aspect of the deposition [79].

Table 5-1 Relevant parameters involved in the sub-processes of electrospray deposition [79]

cone stability	jet break-up droplet size	flight evaporation	deposition film type	parameter origin
flow rate	flow rate		flow rate	
surface tension	surface tension			solvent
		vapor pressure	vapor pressure	solvent
relative permittivity				solvent
				solvent
			concentration	solvent/solute
density	Density	density		solvent/solute
viscosity	Viscosity		viscosity	solvent/solute
conductivity	Conductivity	droplet charge		solvent/solute
		droplet size	droplet size	
			solubility	
		velocity	velocity	
			surface energy	all compounds
			surface structure	substrate
electric field		electric field		setup
spray geometry (nozzle)		spray geometry		setup
coaxial gas flow		coaxial gas flow		setup
		temperature	temperature	setup
		properties medium		

Table 5-1 is not a complete table showing every parameter involved in the electrospray deposition, but a demonstration of how many different factors is involved and how they interact with each other. A brief electrospray model will be presented below summarized from the work of Rietveld *et al.* [79]. The results achieved for this thesis were purely empirical due to the limited control on multiple parameters listed in Table 5-1.

5.2.2. Current Generated in the Cone-Jet

The current during deposition process can be easily measured. A crude model have been formulated, for a flat velocity profile in the jet, by Hartman *et al.* [80] to be used as a prediction for current expected for electrospray:

Equation 5-1
$$I = a_I(KQ\sigma)^{1/2}$$

where a_I is a proportionality constant, K is the conductivity, Q is the flow rate, and σ is the surface tension [79].

5.2.3. Predictions of Droplet Size

According to Hartman *et al.* [80], there are two jet break-up regimes in the cone-jet mode determined by the ratio of the electric stress and the surface tension. If the electric stress is low enough, varicose jet break-up occurs and in such case the diameter of the droplet is determined by:

Equation 5-2
$$d = a_d \left(\frac{\rho \epsilon_o Q^4}{I^2} \right)^{1/6}$$

where a_d , ρ , ϵ_o , are a proportionality constant, density of the solution, and dielectric constant of vacuum respectively. I , current, can be experimentally measured and plugged into the equation.

However, if excessive electric stress exists, whipping jet break-up occurs, which is caused by excess electric surface stress on the jet with respect to the surface tension. If the ratio exceeds ~0.3, Equation 5-2 fails and d needs to be derived using the Rayleigh limit, which is calculated to be [79]:

Equation 5-3

$$d = \left(0.8 \frac{2.88 \epsilon_0 \sigma Q^2}{I^2} \right)^{1/3}$$

5.2.4. Droplet Evaporation

Liquid evaporation is dependent upon many conditions. The basic rate of evaporation of a droplet can be model by assuming that the partial pressure difference between the solvent in the droplet and its environment is the main driving force behind evaporation. The temperature drop of the droplet is also included because this effect is also large secondary contributor. Other effects such as Kelvin effect and the Fuchs effect can be ignored for droplet size on the order of 1 μ m. The rate of evaporation is described by the following equation [79]:

Equation 5-4

$$\frac{\partial d}{\partial t} = \frac{4DM}{R\rho d} \left(\frac{p_c}{T_c} - \frac{p_d}{T_d} \right) f$$

where t is time, D is diffusion of a solvent molecule in air, M is the molar weight of a solvent molecule, R represents the gas constant, ρ is the density of the solution in the droplet, p_c is the vapor pressure of the solvent, T_c is the temperature of the environment, p_d is the vapor pressure of the droplet, and T_d is the temperature of the droplet. For droplet sizes less than 1 μ m, the Reynolds number is small enough for the correction coefficient to be set as $f=1$.

5.2.5. Droplet Charge

The charge of a droplet can be determined based on the current, the fluid flow, and the droplet size. The maximum charge a droplet can hold is dictated by the

Rayleigh limit. The maximum charge for a droplet, q_{max} , is given by the following equation [79]:

Equation 5-5

$$q_{max} = \pi(8\epsilon_0\sigma d^3)^{1/2}$$

in which σ is the liquid surface tension, ϵ_0 is the electric permittivity of free space, and d is the droplet radius. If the droplet achieves this limit, it must expel charges to achieve an unsaturated charge state; of approximately around 80% of the Rayleigh limit. By expelling charges (normally 15%), a portion of the droplet (normally 2%) is expelled with it, increasing the rate that the droplet shrinks.

5.2.6. Droplet Location

To determine the location of the droplet in the axial direction of the spray under an applied electric field, the position of the droplet with respect to time can be modeled by

Equation 5-6

$$\frac{\pi}{6}d^3\rho\frac{dv}{dt} = -3\pi d\mu f_d v + q\vec{E}$$

with v the velocity of the droplet, μ is the viscosity of the medium, f_d a compensation coefficient, and E the electric field. Equation 5-6 can be simplified to

Equation 5-7

$$v = \frac{Eq}{3\pi\mu d}$$

by holding that the droplets are small enough to assume low Reynold's number, therefore $f_d = 1$. In addition, due to the assumed small size, the initial momentum is quickly dominated by the balance of the electric force and the viscous drag force, resulting in the left side of Equation 5-6 to be taken as zero [79].

5.3. Absorption Layer

The sensitivity and the response of the sensor system are highly influenced by the absorption layer which binds chemicals and other analytes to the cantilever surface. The ESD apparatus can be used to deposit various polymers on the surface of the cantilevers. Analyte mass is added to the cantilever due to volumetric absorption or surface binding on this polymer layer.

Polymer coatings are a subset of materials that can be used as a layer of absorption layer on cantilevers. Battiston *et al.* [81] reported on the use of different polymers summarized in Table 5-2 as absorption layers on an array of cantilevers by depositing a 2-3 μm thick polymer layer.

Table 5-2. List of proposed polymers used as absorption layer (adapted from [81])

Coating (5 mg/ml solvent)		Solvent
CMC	Carboxymethylcellulose	Water
PVO	Polyvinylpyridine	Ethanol
PVC	Polyvinylchloride	Acetone
PU	Polyurethane	Dichloromethane
PS	Polystyrene	Toluene
PMMA	Polymethylmethacrylate	Toluene

Polymethylmethacrylate (PMMA) was the chosen absorbing layer due to its well characterized and proven absorbing properties. PMMA has been used as the absorbing layer in humidity, temperature, biological, and chemical sensors. It is easily accessible and is commercially sold in powder form. This material, more commonly known as acrylic glass, is a thermoplastic and transparent plastic that is often used as an alternative to glass due to its light weight and high impact strength.

Table 5-3 Material properties of PMMA

poly(methyl methacrylate) (PMMA)	
Molecular Formula	$(\text{C}_5\text{O}_2\text{H}_8)_n$

Density	1.19g/cm ³
Melting Point	130-140°C
Boiling Point	200.0°C
Dielectric Constant	2.6
Index of Refraction	1.492

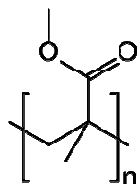


Figure 5.2 Molecular structure of PMMA

PMMA has also been modified in order to change its sensitivity and functionality. For example, Su *et al.* [82] showed that their sensitivity and linearity could be improved by doping PMMA with a mixture of KOH and K₂CO₃. Sarantopoulou *et al.* [83] showed an increase of 400% in volume sorption of alcohol when thin-film PMMA was irradiated using 157 nm laser. A pH sensor was demonstrated by Egami *et al.* [84] by using a methyl-red-doped-PMMA sensor probe.

PMMA polar solvents, required by ESD process, include benzene, toluene, chloroform (anesthetic, carcinogenic 2A), methylene chloride (carcinogenic), esters, ethyl acetate, and amyl acetate. Benzene, chloroform, and methylene chloride are all known carcinogens with serious health risks. Toluene is an attractive alternative due to its relative safety, and is commonly used and proven in literature [85, 86]. Toluene is an aromatic hydrocarbon that is often used as a solvent and can be found in paints, paint thinners, printing ink, glue, and other products. Gasoline also contains 5% to 7% toluene by weight.

Table 5-4 Material properties of toluene

Toluene	
Molecular Formula	C ₇ H ₈ (C ₆ H ₅ CH ₃)
Molar Mass	92.14 g/mol
Density	0.8669 g/mL, liquid
Melting Point	-93 °C

Boiling Point	110.6 °C
Viscosity	0.590 cP at 20°C
Vapor Pressure	3.8kPa at 25°C
Dielectric Constant	2.0-2.4

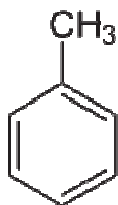


Figure 5.3 Molecular structure of toluene

Proposed analytes of interest include polar molecules such as water and alcohol vapor, apolar molecules such as alkane, and more complex and interesting analytes such as explosive stimulants. Table 5-5 categorizes a list of possible vapors that could be introduced to the chemical sensor.

Table 5-5. List of proposed target analytes

Water (Polar)	Alcohol (Polar)	Alkane (Apolar)	Explosive Stimulants*
Deionized Water	Methanol	Methane	<i>n</i> /TNT
	Ethanol	Ethane	<i>n</i> /RDX
	Propanol	Pentane	<i>n</i> /PETN
	Butanol	Octane	<i>n</i>/KNO₃/- <i>n</i>/KClO₃

5.4. Setup

The ESD setup was assembled using equipment around the lab. It consisted for a high voltage source, a syringe pump, a microliter syringe, a customized metal chip holder, and a conductive collector plane. The metal needle of the syringe was connected to the HV source using an alligator clip. The chip holder was secured on the collector plane which was positioned 1 cm away from the tip of the needle. The collector plate was held at common ground. The electrical fields can be tuned by the voltage source and the flow rate of the ejected solution is controlled by the syringe

pump. PMMA 950 A4 was purchased from MicroChem Corp and dissolved in toluene at a PMMA to toluene ratio of 1:200. Different substrate materials (Si and InP), and surface films (Au and Si₃N₄) were chosen to observe the deposition selectivity between surfaces. Various device structures (plain released waveguides, released cantilevers) were used to investigate the effects of deposition on surface geometries and boundaries. In order to selectively deposit PMMA on active regions of the device, shadow masking was used to allow deposition through a window in the mask. This allows for different deposition runs on different regions of the same chip.

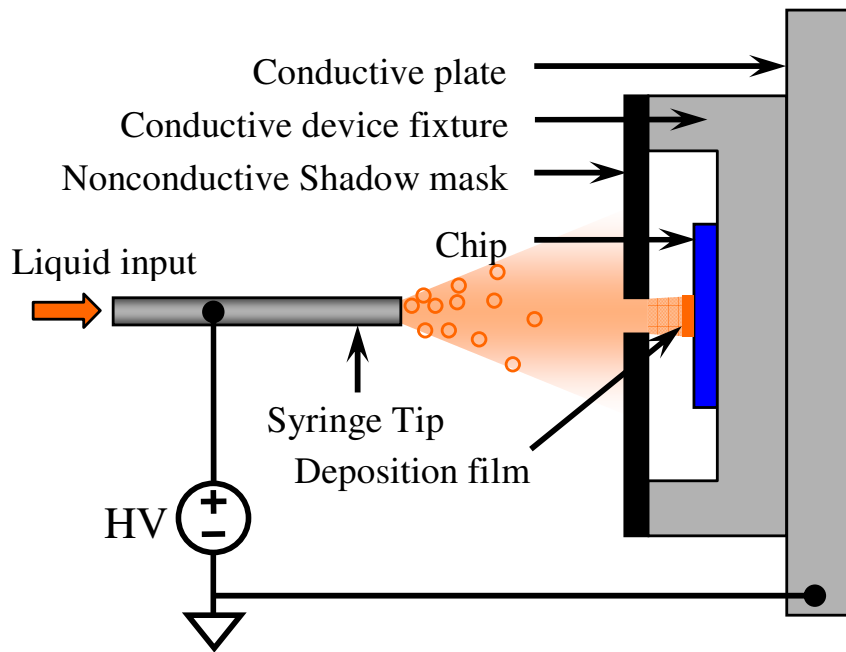


Figure 5.4 Diagram of the ESD setup with a shadow mask defining deposition patterns

5.5. Results

Due to the large numbers of parameters involved in ESD process, many trials were conducted. Parameters, including applied voltage, tip sample distance, deposition time, flow rate, and masking material, were all characterized in order to

achieve a controlled uniform thin-film deposition. The final optimized setup and its deposition results will be detailed below.

A controlled deposition was first achieved on plain silicon chips using a flow rate of 10.8 $\mu\text{l/hr}$, a tip-sample distance of 1 cm apart, and an applied voltage of 7.5 kV. An average surface roughness of 4.5 nm on a 197 nm thick film was measured across a 1 mm profilometer scan. There were thickness non-uniformities across the 2 cm \times 2 cm chip with thickness varying up to $\pm 5\mu\text{m}$. This could be visually observed by the interference patterns on the thin film deposition.

To decrease the non-uniformity across the chip and restrict the deposition region, a shadow mask was applied. A window of 1 mm \times 10 mm was opened in the mask, leaving a deposition region approximately the size of an active region on an InP sensor chip. The average deposition rate of $9.5\pm 5\text{nm/min}$ was calculated based on the thickness of deposited thin film, 47 nm, 94 nm and 143 nm, at three different deposition times 5, 10 , and 15 minutes, respectively. Roughness for each sample ranged from 2 nm to 10 nm. The thickness uniformity across the length of the region was deemed acceptable for cantilever sensor.

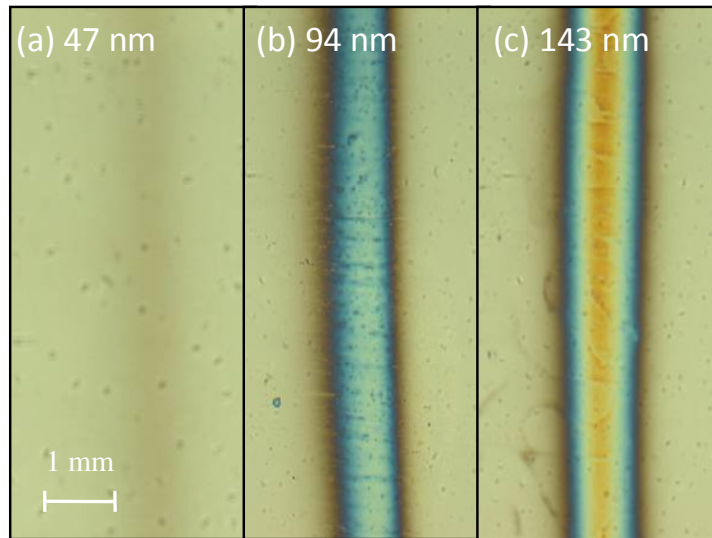


Figure 5.5 Deposition of PMMA at an average rate of 9.5 nm/min on masked chips (a) 5 min (b) 10 min (c) 15 min

PMMA deposition could be extended to other substrates as well. Deposition has been achieved on silicon, silicon nitride, silicon dioxide, gold, and indium phosphide surfaces. No selectivity was observed across different surfaces. However, reduced material deposition was observed on electrically floating structures, such as insulated islands.

Successful deposition had also been achieved on a wide range of surface geometries, including released cantilevers and waveguides. A noticeable increase in deposition film thickness was observed at the edges and corners of structures, which are believed to be caused by edge effects. Enhanced deposition was observed at the edge of conducting structures due to stronger localized electric fields. The film thickness at the edges and corners could increase up to approximately 300% for PMMA deposition. This percentage increase was not uniform, as it is dependent on the geometry. Released devices survived the deposition with no observable damage or stiction issues. This could be attributed to the nanometer sized droplets. These

depositions showed conformal deposition on sidewalls and are assumed to have no coverage on the underside of released structures. Two different suspension heights, 1 μm and 20 μm , underneath the released cantilever were tested. Masking was observed underneath the released structures.

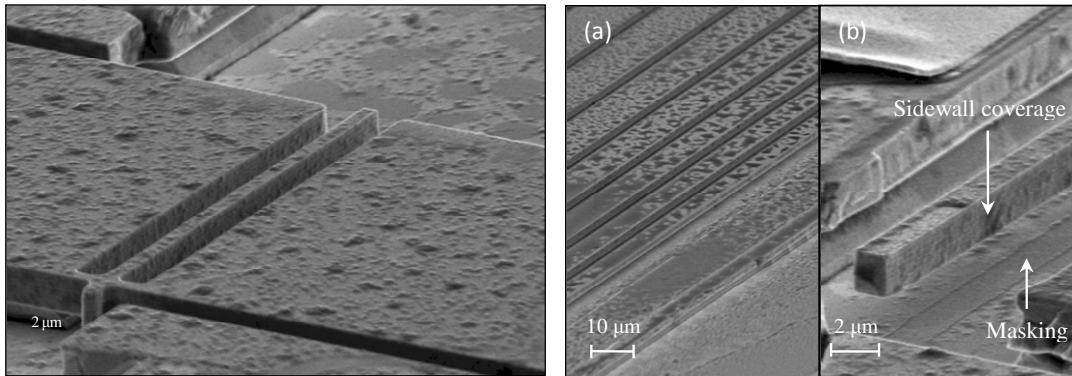


Figure 5.6 SEM images showing conformal coverage of microstructures

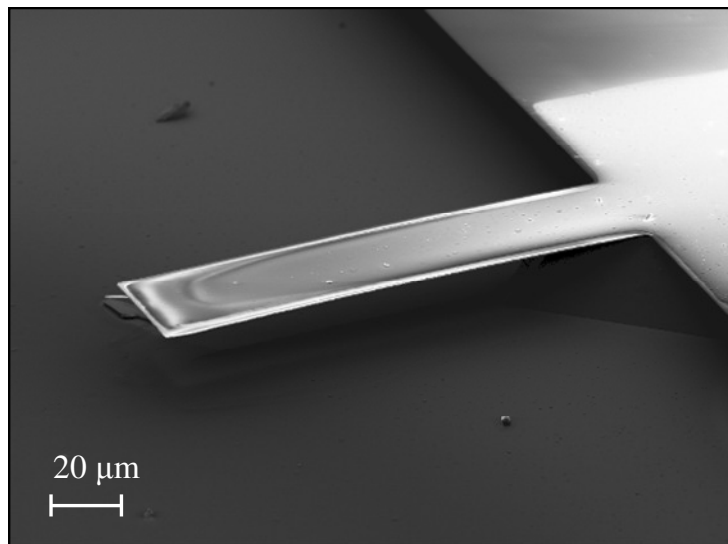


Figure 5.7 SEM image showing increased deposition at the edge of structures due to edge effects

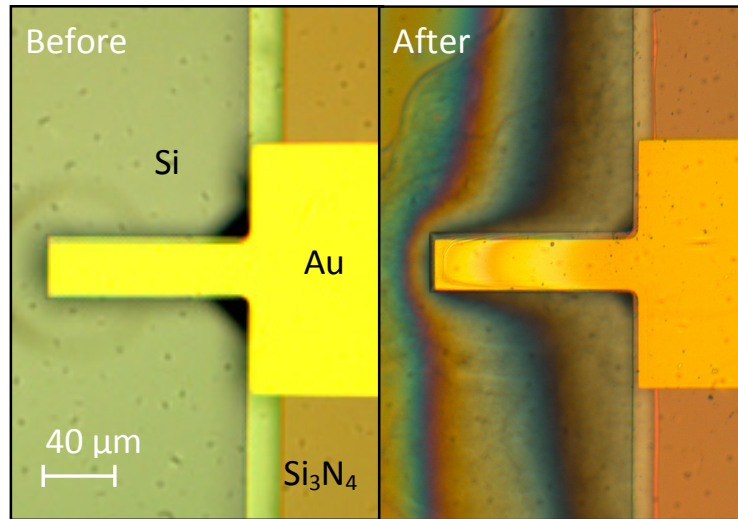


Figure 5.8 Picture of PMMA deposition on various surface materials (Si, Au, and Si₃N₄)

5.6. Discussion

The ESD setup is very simple and inexpensive to construct and easily assembled in any lab that has access to a high voltage source. A microampere supply source should be sufficient for most processes. However the required current for the deposition can be calculated beforehand.

Depositing thin-film receptor layers for cantilever sensor is not a critical process only requiring droplet sizes and film thicknesses are less than a micron. As a result, the ESD is empirically characterized by varying each parameter independently rather than theoretical determination. Ideal conditions were derived by analyzing the deposited film for its uniformity across the film and deposition consistency from run to run. The PMMA solution and deposition process time was kept constant to decrease the number of variables.

The applied voltage and the distance from the tip of the needle to the sample surface were varied to change the magnitude of the electrical field. If the electrical field was too low, usually below 5×10^5 V/m, negligible PMMA was deposited onto

the surface after a 15 min deposition period. The current supplied by the source was typically below $10\mu\text{A}$. If the electrical field was too high, above $8.5\times 10^5\text{ V/m}$, arcing between the conducting tip and the chip surface occurred, resulting from the breakdown of air. The current supplied reached the maximum level ($250\mu\text{A}$) and resulted in the termination of the deposition process. The thin-film deposition occurred between $5\times 10^5\text{ V/m}$ to $8.5\times 10^5\text{ V/m}$. The film thickness and uniformity could be controlled to a certain extent by changing the flow rate and the electric field. Increasing the flow rate caused the deposition rate to increase but thickness non-uniformity increased as well. Thickness non-uniformity could be observed from the interference patterns.

Although the empirical characterization of the ESD system was relatively simple, consistency was difficult to achieve. During the process of characterizing the system, it was discovered that the ESD system is very sensitive to environmental conditions. An example of this is a decreased break down voltage at a higher ambient humidity.

Ideally, the ESD system should be setup in a cleanroom environment where the particle count is low. This is because any particle that enters the high electrical field will be swept towards the surface. The accumulation of particles can cause failure of devices, decreasing the yield.

Conclusion and Future Work

6.1. Summary of Results

This thesis research demonstrated the enhancement of an InP resonator sensor through the development of an adaptive feedback circuit and electrospray deposition. The feedback circuit developed can be integrated with a wide range of resonators to autonomously detect and track resonant frequency of resonators without tailoring to individual devices by implementing a hill climbing algorithm with discreet electronic components. The hill climbing algorithm does not require a phase relationship between the input and output signal, eliminating the need for phase or amplitude compensation stages. The feedback circuit was designed, built, and tested. Sensitivity and repeatability of the system were analyzed and the results were related to sensing applications.

The electrospray deposition developed is a thin-film deposition method that is used as a post-processing on microstructures. Due to its generation of ultra-small droplets, it can deposit high-uniformity thin-films receptors on suspended structures, such as released resonators sensors. Deposition of a receptor layer on released structures is challenging due to stiction and material compatibility issues. Deposition of different receptor layers on a single chip is even more difficult due to further complications. The successful demonstration of this deposition method allows for the use of novel receptor layers for resonators sensors, increasing the versatility of the resonator sensor platform.

6.1.1. Resonator Feedback Circuit

The feedback system presented here is a simple alternative design to existing feedback circuit design. The feedback circuit locates and tracks the resonant peak by implementing a hill climbing algorithm, an optimization technique. The algorithm is implemented using four-stage feedback circuit consisting of an amplitude detector, a differentiator, a digital logic circuit, and a voltage controlled oscillator (VCO). The feedback circuit receives the cantilever displacement output and supplies the actuation signal to the resonator from the VCO output, a constant amplitude periodic signal. The VCO's output frequency is set by the input voltage of the VCO, established by the digital logic circuit which determines the cantilever's maximum amplitude response. By monitoring the VCO input voltage, the resonant frequency with respect to time can be measured, and hence the change in mass of the cantilever.

The hill climbing algorithm implementation has been modeled with PSPICE and confirmed by open-loop circuit board testing. A single feedback circuit was then used in closed-loop scheme to detect eight different cantilevers (width = 1.4 μm , length = 40-75 μm , and thickness = 1.6 μm), resonating at 201 kHz to 592 kHz in ambient conditions. This search algorithm has no inherent limitations in resonant frequency range and shift detection but the feedback circuit is limited due to electronics performance. A resonator measured with this system yields an 11.8 Hz minimum standard deviation of averaged resonant frequency. This corresponds to a mass resolution limit of 123 fg for this device.

The adaptability and precision of the feedback circuit to detect the resonant frequency of resonators is ultimately limited by electronic components. The

sensitivity of the system is dependent on the noise level and time delay of the system. The integration of this universal feedback circuit with resonator devices allows for more flexible real-time readout and enables the development of smart chip-scale microsystems. This circuit can also be applied to other applications in the field of microsystems such as 3D MEMS fiber aligners [94], tunable lasers [95], and optical filters [96].

6.1.2. Electro spray Deposition

PMMA thin-film, used as a receptor layer, was deposited on various MEMS devices and substrates by an electro spray deposition setup that was empirically characterized to achieve repeatability. Electro spraying utilizes electrohydrodynamic forces to create a shear stress on a liquid droplet's surface. All deposition parameters were empirically determined. PMMA, dissolved in toluene, was deposited under high electrical field (7.1kV/cm) between the syringe and the collector. Different substrate materials (Si and InP), and surface films (Au and Si₃N₄) were chosen to observe the deposition selectivity between surfaces. At a flow rate of 10.8 μl/hr, the average deposition rate was 9.5±5 nm/min on masked samples, with no observable selectivity. An average surface roughness of 4.5 nm on a 197 nm thick film was measured across 1 mm. PMMA deposition can be extended to other deposition materials with polar solvents [78]. Different devices (Si waveguides, released Si₃N₄ and InP cantilevers) were chosen to characterize the deposition properties on different structure sizes and geometries. Released devices survived the deposition with no observable damage and stiction issues, due to the nanometer sized droplets. Although uniformity was not achieved across a cantilever, electro spray deposition of PMMA receptor layers on

various cantilevers was sufficient for sensing applications. The simplicity of the setup and its potential for depositing different films can enable the deposition of a wide range of receptor layers often incompatible with standard fabrication processes and facilitate the fabrication and increase the versatility of many MEMS released devices, such as resonator sensors.

6.2.Future Work

The work developed in this thesis was a proof of concept that demonstrated the feasibility of an adaptive feedback circuit and electrospray deposition of thin-film on resonators. These components can be further optimized and will ultimately be implemented in a resonator sensor microsystem. Below are some key points that will be addressed in future works.

- 1) The feedback circuit's minimum standard deviation is 11.8 Hz, corresponding to a minimum mass detection of 123 fg. To improve the sensitivity of the resonator sensor system, the standard deviation needs to be reduced. The feedback circuit can be further optimized by decreasing the output signal's delay time, thus decreasing amplitude of oscillation around the peak resonance, and the overall system noise. These issues can be dramatically reduced if the feedback circuit was implemented on a printed circuit board or on-chip. Shrinking the size of the devices will decrease parasitic affects, noise, and delays. The feedback circuit frequency response and the output signal to noise ratio are all expected to increase. A final step of 3-D chip-scale integration of the sensor systems could be

- carried out using flip-chip bonding technology to decrease parasitic effects of interconnects.
- 2) One of the limiting factors in the operation range of the feedback circuit is low optical signal received from the photodetector. If the signal to noise ratio of the input signal drops below a threshold level, the feedback circuit cannot implement the hill climbing algorithm appropriately. To increase the operation range of the circuit, the optical signal intensity from the resonator device needs to be enhanced by reducing the optical loss in the resonator system. Optical loss can be reduced dramatically by using the III-V material to implement an on-chip optical source and detector [14] to eliminate coupling loss at the input and output. Optical loss due to misalignment and dispersion will be eliminated. Waveguide scattering losses can be reduced by improving waveguide sidewall roughnesses. This can be achieved through improved etching process such as using an inductively coupled plasma tool [97]. Lastly, residual stress needs to be balanced to ensure horizontal alignment between the cantilever waveguide and collector waveguide, to maximize coupling.
 - 3) The purpose of this research is to enhance the functionality of a microsensor system. Chemical vapor sensing will need to be conducted by: (1) using the thin-film PMMA deposited by electrospray deposition and (2) tracking the resonant frequency with the feedback circuit. Organic vapors can be introduced to the system via nitrogen carrier gas. By monitoring the shift in resonant frequency, the change in mass can be deduced with respect to time. Organic vapors, such as isopropyl alcohol and methanol, are often used in literature [14] due to their

relatively safe and inert properties and high vapor pressure at room condition. Absorption and desorption properties of PMMA will be determined based on the rate of increase or decrease of the resonant frequency shift. Complete desorption and repeatability of sensing measurements will be evaluated. Additionally, detection of different concentrations of organic vapor will be investigated to determine if there is any absorption and desorption dependence with respect to vapor concentration.

Bibliography

- [1] W. W. Judy, "Microelectromechanical Systems (MEMS): Fabrication, Design and Applications," *Smart Materials and Structures*, vol. 10, pp. 1115-1134, 2000.
- [2] M. Rabaey, "A 300umW 1.9GHz CMOS oscillator utilizing micromachined resonators," presented at Proceedings of the 28th European Solid-State Circuits Conference 2002, 2002.
- [3] J. J. Yao, "RF MEMS from a device perspective," *Journal of Micromechanical and Microengineering*, vol. 10, pp. R9-R38, 2000.
- [4] N. V. Lavrik, M. J. Sepaniak, and P. G. Datskosa, "Cantilever transducers as a platform for chemical and biological sensors," *Review of Scientific Instruments*, vol. 75, pp. 2229-53, 2004.
- [5] O. B. H. Baltes, A. Hierlemann, D. Lange, and C. Hagleitner, "CMOS MEMS - present and future," presented at Proceedings of the Fifteenth IEEE International Conference on Micro Electro Mechanical Systems, Las Vegas, NV, USA, 2002.
- [6] Y. Lee, G. Lim, and W. Moon, "A self-excited micro cantilever biosensor actuated by PZT using the mass micro balancing technique," *Sensors and Actuators A (Physical)*, vol. 130-131, pp. 105-110, 2006.
- [7] J. Tamayo, R. Owen, and M. Miles, "High-Q Dynamic Force Microscopy in Liquid and Its Application to Living Cells," *Biophysical Journal*, vol. 81, pp. 526-537, 2001.
- [8] J. Tamayo, "Study of the noise of micromechanical oscillators under quality factor enhancement via driving force control," *Journal of Applied Physics*, vol. 97, pp. 44903, 2005.
- [9] J. Acramone, F. Serra-Graells, M. Boogaart, J. Brugger, F. Torres, G. Abadal, N. Barniol, and F. Perez-Murano, "A Compact and Low-Power CMOS Circuit for Fully Integrated NEMS Resonators," *IEEE Transactions on Circuits and Systems—II: Express Briefs*, vol. 54, pp. 377-381, 2007.
- [10] E. Edvardsen, B. Hok, and T. Ytterdal, "A CMOS Analog Integrated Circuit for Actuation and Readout of a MEMS CO₂ Sensor," presented at Proceedings of Norchip Conference, 2004.
- [11] G. K. Fedder, "CMOS MEMS Oscillator for Gas Chemical Detection," presented at Proceedings of IEEE Sensors 2004, 2004.
- [12] Y. Li, C. Hagleitner, J. Lichtenberg, O. Brand, and H. Baltes, "Very High Q-Factor in Water Achieved by Monolithic Cantilever Sensor with Fully Integrated Feedback," presented at Proceedings of IEEE Sensors Conference 2003, 2003.
- [13] C. Vancura, K. Kirstein, F. Josse, A. Hierlemann, and J. Lichtenberg, "Fully Integrated CMOS Resonant Cantilever Sensor for Bio-Chemical Detection in Liquid Environments," presented at Proceedings of the 13th International Conference on Solid-State Sensors, Actuators and Microsystems, Seoul, Korea.

- [14] N. Siwak, "Indium Phosphide MEMS Cantilever Waveguides for Chemical Sensing with Integrated Optical Readout," in *Electrical and Computer Engineering*, vol. Master of Engineering. College Park: University of Maryland, 2007.
- [15] G. Taylor, "Disintegration of Water Drops in an Electric Field," *Proceedings of the Royal Society of London. Series A, Mathematical and Physical Sciences (1934-1990)*, vol. 280, pp. 383, 1964.
- [16] J. B. Fenn, M. Mann, C. K. Meng, S. F. Wong, and C. M. Whitehouse, "Electrospray ionization for mass spectrometry of large biomolecules," *Science*, vol. 246, pp. 64, 1989.
- [17] P. M. Martinez-Sanchez, "Lecture 23-25: Colloidal Engines," MIT.
- [18] K. E. Petersen, "Silicon as a mechanical material," *Proceedings of the IEEE*, vol. 70, pp. 420, 1982.
- [19] R. S. Muller, "MEMS: Quo Vadis in Century XXI," *Microelectronic Engineering*, vol. 53, pp. 47-54, 2002.
- [20] R. C. Jaeger, *Introduction to Microelectronic Fabrication*, vol. V. Upper Saddle River, New Jersey: Prentice hall, 2002.
- [21] T. J. Suleski and R. D. T. Kolste, "Fabrication trends for free-space microoptics," *Journal of Lightwave Technology*, vol. 23, pp. 633, 2005.
- [22] H. Fujita and H. Toshiyoshi, "Optical MEMS," *IEICE Trans. Elec.*, vol. E83, pp. 1427-1434, 2000.
- [23] L. J. Hornbeck, "Current status of the digital micromirror device (DMD) for projection television applications," in *International Electron Devices Meeting 1993. Technical Digest (Cat. No.93CH3361-3)*. New York, NY: IEEE Electron Devices Soc. IEEE, 1993, pp. 381.
- [24] O. S. Corporation, "Overview of the Digital Micromirror Device."
- [25] D. J. Bishop, C. R. Giles, and G. P. Austin, "The Lucent LambdaRouter: MEMS technology of the future here today," *IEEE Commun. Mag.*, vol. 40, pp. 75-79, 2002.
- [26] M. Xiaohua, "Optical switching technology comparison: optical MEMS vs. other technologies," *IEEE communications magazine*, vol. 41, pp. S16, 2003.
- [27] E. Ollier, "Optical MEMS devices based on moving waveguides," *IEEE Journal on Selected Topics in Quantum Electronics*, vol. 8, pp. 155-162, 2002.
- [28] T. Bakke, C. P. Tigges, J. J. Lean, C. T. Sullivan, and O. B. Spahn, "Planar microoptomechanical waveguide switches," *IEEE Journal of Selected Topics in Quantum Electronics*, vol. 8, pp. 64-72, 2002.
- [29] M. W. Pruessner, M. Datta, K. Amarnath, S. Kanakaraju, and R. Ghodssi, "Indium Phosphide Based MEMS End-Coupled Optical Waveguide Switches," presented at 17th International Indium Phosphide and Related Materials Conference, Glasgow, Scotland, 2005.
- [30] M. W. Pruessner, K. Amarnath, M. Datta, D. Kelly, S. Kanakaraju, P.-T. Ho, and R. Ghodssi, "InP-Based Optical Waveguide MEMS Switches with Evanescent Coupling Mechanism," *Journal of Microelectromechanical Systems*, vol. 14, pp. 1070-81, 2005.

- [31] M. L. Povinelli, Solomon Assefa, Steven G. Johnson, Shanhui Fan, A. A. Erchak, G. S. Petrich, E. Lidorikis, J. D. Joannopoulos, L. A. Kolodziejski, and E. P. Ippen, "Design of a Nanoelectromechanical High-Index-Contrast Guided-Wave Optical Switch for Single-Mode Operation at 1.55 μm ," *IEEE Photonics Technology Letters*, vol. 15, pp. 1207-1209, 2003.
- [32] H. Yamaguchi, S. Miyashita, and Y. Hirayama, "Microelectromechanical displacement sensing using InAs/AlGaSb heterostructures," *Applied Physics Letters*, vol. 82, pp. 394, 2003.
- [33] T. Andreas R. Stonasa, Steven P. DenBaars,c, and Evelyn L. Hua, "Development of gallium nitride-based MEMS Structures," presented at Transducers 2003, Boston, MA.
- [34] C. Kittel, *Introduction to Solid State Electronics*, 7th ed. New York: John Wiley and Sons, 1996.
- [35] M. R. Leys, "Fundamental growth kinetics in MOMBE/CBE, MBE and MOVPE," *Journal of Crystal Growth*, vol. 209, pp. 225-231, 2000.
- [36] N. Siwak, *Indium phosphide optical MEMS for chemical and biological sensing 2006 IEEE/NLM Life Science Systems and Applications Workshop*, 2006.
- [37] K. Hjort, "Sacrificial etching of III–V compounds for micromechanical devices," *Journal of Micromechanics and Microengineering*, vol. 6, pp. 370-375, 1996.
- [38] E. F. Schubert, "Physical Foundations of Solid-State Devices," 2006.
- [39] H. Kunzel, R. Kaisser, S. Malchow, and S. Schelhase, "Status of InP-Based Metal Organic MBE with Reference to Conventional MBE and MOVPE," presented at Proceedings of 2001 International conference on Indium Phosphide and related materials, Nara, Japan, 2001.
- [40] T. Bakke, C. P. Tigges, and C. T. Sullivan, "1x2 MOEMS switch based on silicon-on-insulator and polymeric waveguides," *Electronics Letters*, vol. 38, pp. 177-178, 2002.
- [41] H. C. Nathanson, W. E. Newell, R. A. Wickstrom, and R. J. J. Davis, "The resonant gate transistor," *IEEE Transactions on Electron Devices*, vol. ED-14, pp. 117-133, 1967.
- [42] R. T. Howe and R. S. Muller, "Resonant microbridge vapor sensor," *IEEE Transactions on Electron Devices*, vol. ED-33, pp. 499-506, 1986.
- [43] P. Kumar, L. Lihua, L. Calhoun, P. Boudreaux, and D. DeVoe, "Fabrication of piezoelectric Al/sub 0.3/Ga/sub 0.7/As microstructures," *Sensors and Actuators A (Physical)*, vol. A115, pp. 96, 2004.
- [44] T. D. S. Kevin Y. Yasumura, Eugene M. Chow, Timothy Pfafman, Thomas W. Kenny, Barry C. Stipe, and Daniel Rugar, "Quality Factors in Micron- and Submicron-Thick Cantilevers," *Journal of Microelectromechanical Systems*, vol. 9, pp. 117-125, 2000.
- [45] J. H. Smith, "Micromachined pressure sensors: review and recent developments," *Smart Materials and Structures*, vol. 6, pp. 530-539, 1997.
- [46] N. V. Lavrik and P. G. Datskosa, "Femtogram mass detection using photothermally actuated nanomechanical resonators," *Applied Physics Letters*, vol. 82, pp. 2697-9, 2003.

- [47] J. Hietanen, J. Bomer, J. Jonsmann, W. Olthuis, P. Bergveld, and K. Kaski, "Damping of a vibrating beam," *Sensors and Actuators A*, vol. 86, pp. 39-44, 2000.
- [48] K. Ikeda, H. Kuwayama, T. Kobayashi, T. Watanabe, T. Nishikawa, T. Yoshida, and K. Harada, "Silicon pressure sensor integrates resonant strain gauge on diaphragm," *Sensors and Actuators*, vol. A21-23, pp. 146-150, 1990.
- [49] S. Amy, C. R. Grayson, A. M. Johnson, N. T. Flynn, Y. LI, M. J. Cima, and R. Langer, "A BioMEMS Review: MEMS Technology for Physiologically Integrated Devices," presented at Proceedings of the IEEE, 2004.
- [50] S. D. Don C Abeysinghe, Howard E Jackson, and Joseph T Boyd, "Novel MEMS pressure and temperature sensors fabricated on optical fibers," *Journal of Micromechanical and Microengineering*, vol. 12, pp. 229-235, 2002.
- [51] G. Stemme, "Resonant silicon sensors," *Journal of Micromechanics and Microengineering*, vol. 1, pp. 113, 1991.
- [52] S. T. Koev, H. Yi, L-Q. Wu, W. E. Bentley, G. W. Rubloff, G. F. Payne, and R. Ghodssi, "Mechano-transduction of DNA Hybridization and Dopamine Oxidation through Electrodeposited Chitosan Network," *Lab on a Chip (LOC)*, vol. 7, pp. 103-111, 2007.
- [53] X. Luo, H. Yi, G. F. Payne, R. Ghodssi, W. E. Bentley, and G. W. Rubloff, "Programmable Assembly of a Metabolic Pathway Enzyme in a Pre-packaged Reusable BioMEMS Device," *Lab on a Chip (LOC)*, vol. 8, pp. 420-430, 2008.
- [54] B. Illic, D. Czaplewski, M. Zalalutdinov, H. G. Craighead, P. Neuzil, C. Campagnolo, and C. Batt, "Single cell detection with micromechanical oscillators," *Journal of Vacuum Science and Technology*, vol. B19, pp. 2825-8, 2001.
- [55] T. Lewandowski, X. Luo, G. F. Payne, R. Ghodssi, G. W. Rubloff, and W. E. Bentley, "Protein Assembly onto Microfabricated Devices through Enzymatic Activation of Fusion Pro-tag," *Biotechnology and Bioengineering*, vol. 99, pp. 499-507, 2008.
- [56] T. Gotszalk, P. B. Grabienc, P. Dumania, F. Shi, P. Hudek, and IW. Rangelow, "Fabrication of multipurpose piezoresistive Wheatstone bridge cantilevers with conductive microtips for electrostatic and scanning capacitance microscopy," *Journal of Vacuum Science and Technology B*, vol. 16, pp. 3948-3953, 1998.
- [57] J. Soderkvist and K. Hjort, "Flexural vibrations in piezoelectric semi-insulating GaAs," *Sensors and Actuators A (Physical)*, vol. A39, pp. 133.
- [58] D. L. DeVoe, "Piezoelectric thin film micromechanical beam resonators," *Sensors and Actuators A*, vol. 88, pp. 263-272, 2001.
- [59] L. K. Baxter, *Capacitive Sensors, Design and Applications*. New York: IEEE Press, 1997.
- [60] L. A. Pinnaduwege, V. Boiadjev, J. E. Hawk, and T. Thundat, "Sensitive detection of plastic explosives with self-assembled monolayer-coated microcantilevers," *Applied Physics Letters*, vol. 83, pp. 1471-3, 2003.
- [61] B. I. Kim, "Direct comparison between phase locked oscillator and direct resonance oscillator in the noncontact atomic force microscopy under

- ultrahigh vacuum," *Review of Scientific Instruments*, vol. 75, pp. 5035-5037, 2004.
- [62] D. M. Vittorio Ferrari, Andrea Taroni, Elisabetta Ranucci, and Paolo Ferruti, "Development and Application of mass Sensors Based on Flexural Resonances in Alumina Beams," presented at IEEE Transactions on Ultrasonics, Ferroelectrics, and Frequency Control, 1996.
- [63] F. Lochon, L. Fadel, I. Dufour, D. Rebière, and J. Pistré, "Silicon made resonant microcantilever- Dependence of the chemical sensing performances on the sensitive coating thickness," *Materials Science and Engineering C*, vol. 26, pp. 348-353, 2006.
- [64] J. H. Smith, and J. J. Sniegowski, "Material and processing issues for the monolithic integration of microelectronics with surface-micromachined polysilicon sensors and actuators," presented at Proceedings of SPIE, 1995.
- [65] P. J. McWhorter, "The broad sweep of integrated," *IEEE Spectrum*, pp. 24-33, 1998.
- [66] B.-H. Willfried Bair, Rao R. Tummala, Ritwik Chatterjee, and Eric Beyne, "Silicon Interposers Wait for an Application," *I-Micronews*, 2008.
- [67] S. D. Senturia, *Microsystem Design*. Boston, MA: Kluwer Academic, 2000.
- [68] D. Marcuse, "Tilt, Offset, and End-Separation Loss of Lowest-Order Slab Waveguide Mode," *Journal of Lightwave Technology*, vol. LT-4, pp. 1647-1650, 1986.
- [69] R. Berger, C. Gerber, H. P. Lang, and J. K. Gimzewski, "Micromechanics: a toolbox for femtoscale science: "Towards a laboratory on a tip"," *Microelectronic Engineering*, vol. 35, pp. 373-379, 1997.
- [70] M. F. Mabrook, C. Pearson, and M. C. Petty, "Inkjet-printed polymer films for the detection of organic vapors," *IEEE Sensors Journal*, vol. 6, pp. 1435-1444, 2006.
- [71] D. Mandler, "Studying the binding of Cd²⁺ by ω-mercaptoalkanoic acid self assembled monolayers by cyclic voltammetry and scanning electrochemical microscopy (SECM)," *Journal of Electroanalytical Chemistry*, vol. 581, pp. 310-319, 2005.
- [72] D. L. Allara, "Critical issues in applications of self-assembled monolayers," *Biosensors and Bioelectronics*, vol. 10, pp. 771, 1995.
- [73] Y.-H. Kim, K. Jang, Y. J. Yoon, and Y.-J. Kim, "A novel relative humidity sensor based on microwave resonators and a customized polymeric film," *Sensors and Actuators B*, vol. 117, pp. 315-322, 2006.
- [74] I. Voiculescu, M. E. Zaghoul, R. A. McGill, E. J. Houser, and G. K. Fedder, "Electrostatically Actuated Resonant Microcantilever Beam in CMOS Technology for the Detection of Chemical Weapons," *IEEE Sensors Journal*, vol. 5, pp. 641-647, 2005.
- [75] Z. Th. Wink, A. Bult, and W. P. van Bennekom, "Self-assembled Monolayers for Biosensors," *Analyst*, vol. 122, pp. 43R-50R, 1997.
- [76] Hars, aacute, and G. nyi, "Polymer films in sensor applications: a review of present uses and future possibilities," *Sensor Review*, vol. 20, pp. 98, 2000.
- [77] G. Harsányi, *Polymer films in Sensor Applications*: CRC Press, 1995.

- [78] A. Jaworek, "Electrospray droplet sources for thin film deposition," *Journal of Materials Science*, vol. 42, pp. 266-297, 2007.
- [79] K. K. Ivo, B. Rietveld, H. Yamada, and K. Matsushige, "Electrospray Deposition, Model, and Experiment: Toward General Control of Film Morphology," *Journal of Physical Chemistry B*, vol. 110, pp. 23351-23364, 2006.
- [80] A. Hartman, D. J. Brunner, D. M. A. Camelot, J. C. M. Marijnissen, and B. Scarlett, "ELECTROHYDRODYNAMIC ATOMIZATION IN THE CONE-JET MODE PHYSICAL MODELING OF THE LIQUID CONE AND JET," *Journal of Aerosol Science*, vol. 30, pp. 823, 1999.
- [81] F. M. Battiston, J. P. Ramseyer, H. P. Lang, M. K. Baller, C. Gerber, J. K. Gimzewski, E. Meyer, and H. J. Guntherodt, "A chemical sensor based on a microfabricated cantilever array with simultaneous resonance-frequency and bending readout," Switzerland, 2001.
- [82] Y.-L. S. Pi-Guey Su, Chu-Chieh Lin, "Humidity sensor based on PMMA simultaneously doped with two different salts," *Sensors and Actuators B*, vol. 113, pp. 883-886, 2006.
- [83] E. Sarantopoulou, A.C. Cefalas, K. Manoli, M. Sanopoulou, D. Goustouridis, S. Chatzandroulis, I. Raptis, "Surface nano/micro functionalization of PMMA thin films by 157 nm irradiation for sensing applications," *Applied Surface Science*, vol. 254, pp. 1710-1719, 2008.
- [84] C. Egami, M. Isai, M. Ogita, "Evanescent-wave spectroscopic fiber optic pH sensor," *Optics Communications*, vol. 122, pp. 122-126, 1996.
- [85] N.-E. L. Sanghun Shin, Joon-Shik Park, Hyo-Derk Park, and Jaichan Lee, "Piezoelectrically Driven Self-Excited Microbridge VOCs Sensor," *Ferroelectrics*, vol. 338, pp. 41-47, 2006.
- [86] R. Capan, A. K. hassen, and T. Tanrisever, "Poly(methyl methacrylate) films for organic vapour sensing," *Journal of Physics D: Applied Physics*, vol. 36, pp. 1115-1119, 2003.
- [87] B. Xi, Z. Liu, C. H. Xia, L. Zhang, "A Smart Hill-Climbing Algorithm for Application Server Configuration," presented at Proceedings of WWW2004, New York, Ny, USA, 2004.
- [88] S. Zeng, G. Chen, H. Garis, L. Kang, L. Ding, "Orthogonal Dynamic Hill-Climbing Algorithm for Dynamic Optimization Problems," presented at Proceedings of 2006 IEEE Congress on Evolutionary Computation, 2006.
- [89] D. Miller, "An Iterative Hill climbing Algorithm for Discrete Optimization on Images: Application to Joint Encoding of Image Transform Coefficients," *IEEE Signal Processing letters*, vol. 9, pp. 46-50, 2002.
- [90] D. S. Johnson, *Computers and Intractability: A Guide to the Theory of NP-Completeness*. New York: Freeman, 1979.
- [91] N. Russell, Peter, *Artificial Intelligence: A Modern Approach*, 2nd ed. Upper Saddle River, NJ: Prentice Hall, 2003.
- [92] D. Peters, C. Marschner, O. Nussen, and R. Laur, "Enhanced Optimization Algorithms for the development of Microsystems."

- [93] T. Bifano, "Optics Calibration for a Wide-field Microscope," presented at Proceedings of the SPIE – The International Society for Optical Engineering 2008, San Jose, CA, USA, 2008.
- [94] B. Morgan, and R. Ghodssi, "Automated 2-Axis Optical Fiber Alignment using Gray-scale Technology," *Journal of Microelectromechanical Systems (JMEMS)*, vol. 16, pp. 102-110, 2007.
- [95] Q. Liu, D. Y. Tang, and C. Lu, "Tunable laser using micromachined grating with continuous wavelength tuning," *Applied Physics Letters*, vol. 85, pp. 3684-3686, 2004.
- [96] M. Datta, M. W. Pruessner, D. Kelly, and R. Ghodssi, "Design of MEMS-Tunable Novel Monolithic Optical Filters in InP with Horizontal Bragg Mirrors," *Solid State Electronics*, vol. 48, pp. 1959-1963, 2004.
- [97] J. Lin, "Smooth and vertical-sidewall InP etching using Cl_2/N_2 inductively coupled plasma," *Journal of Vacuum Science and Technology B*, vol. 22, pp. 510-512, 2004.